M2LW-21OR0402023

Light Water Reactor Sustainability Program

Toward an understanding of straining mode, grain boundary oxidation and localized deformation on intergranular cracking of neutron irradiated austenitic stainless steels in pressurized water reactor relevant conditions

September 2021

U.S. Department of Energy

Office of Nuclear Energy

M2LW-21OR0402023

Toward an understanding of straining mode, grain boundary oxidation and localized deformation on intergranular cracking of neutron irradiated austenitic stainless steels in pressurized water reactor relevant conditions

Gary S. Was (Principal Investigator)
Srinivasan Swaminathan
Kai Sun
Donghai Du

September 2021

Prepared for the
U.S. Department of Energy
Office of Nuclear Energy

SUMMARY

The main objective of this LWRS project is to identify the mechanism of irradiation-assisted stress corrosion cracking (IASCC) in highly irradiated solution-annealed 304 and cold-worked 316 stainless steels in PWR primary water environment and to recommend mitigation strategies. The four-point bend test was used to determine the crack initiation stress and then, to identify the microstructure features responsible for IASCC initiation. For this purpose, specimens from CW316 SS (dose levels: 42, 46.9, 67.4 and 125.4 dpa) and SA304 SS (dose levels: 5.4, 69, 95 and 125.4 dpa) irradiated in BOR-60 reactor in Russia, were selected for analysis in the Irradiated Materials Testing Lab (IMTL) at the University of Michigan. To determine the parameters governing IASCC, single and/or interrupted straining four-point bend tests, constant load mode, and pre-oxidation in PWR primary water with subsequent straining in high temperature argon gas were conducted.

KEY FINDINGS

- The four-point bend tests in single straining and interrupted straining modes revealed that the stress to crack initiation in intermediate irradiation dose (42 dpa) CW316 SS specimen is 0.5YS whereas in low dose (5.4 dpa) SA304 SS specimen cracks formed at 0.6YS. These tests were carried out at constant strain rate of 4.3×10^{-8}/s.
- Four-point bend tested specimens SA304 SS (of dose levels 5.4 and 95 dpa) at constant strain rate in PWR primary water resulted IG cracking at 0.6YS, whereas the constant load tests for 200h of samples with the same dose and in the same environment initiated cracks at a lower stress of 0.5YS.
- A key observation is the formation of oxidized grain boundaries that preceded crack initiation. The grain boundaries become progressively more oxidized with exposure time, and oxidized grain boundaries cracked preferentially to non-oxidized grain boundaries.
- To separate the effect of grain boundary oxidation on IG cracking, pre-oxidation of a SA304 SS (69 dpa) in PWR primary water for 210 h was carried out without application of load, followed by straining in high temperature Ar. IG cracking occurred at a stress level of 0.5YS compared to 0.8YS for a sample with the same dose strained in PWR primary water. This result establishes the oxidation of the grain boundary as the process driving susceptibility to IG cracking.
- No cracks were observed upon straining of an irradiated sample in high temperature argon gas, confirming that grain boundary must be oxidized for it to be susceptible to IG cracking.
- The intersection site of a dislocation channel and an oxidized grain boundary is the most effective in inducing intergranular cracking as IG cracks preferably form at such sites. Very few IG cracks were found on GBs that did not contain such sites.
- Post-test analysis revealed that IG cracks in oxidized grain boundaries form in the oxide and not at the oxide-metal interface, indicating that it is the oxide that is the weaker structure and most prone to fracture.

ACKNOWLEDGEMENT

This project was co-founded by DOE under the Light Water Reactor Sustainability (LWRS) program (Contract 4000136608) and EPRI (Contract 10010367). The authors would like to thank Connor Shamberger for assistance in the Irradiated Materials Testing Laboratory at the University of Michigan. Gratitude is also extended to Dr. Maxim Gussev, Patricia Tedder, Jesse Werden and other technical support staff at Oak Ridge National Laboratory for assistance with specimen handling and preparation.

Contents

FIGURES

TABLES

ACRONYMS

ASTM	American Society of Testing and Materials
BWR	boiling water reactor
BSE	backscattered electron
CERT	constant extension rate tensile
CW	cold-work
DC	dislocation channel
DO	dissolved oxygen
EBSD	electron back-scattered diffraction
EDS	energy-dispersive X-ray spectroscopy
EDM	electron discharge machining
EELS	electron energy loss spectroscopy
EPRI	Electric Power Research Institute
FWHM	full width at half maximum
HAADF	High angle annular dark field
HAGB	High angle grain boundary
HR	high resolution
GB	grain boundary
IASCC	irradiation assisted stress corrosion cracking
IG	intergranular
IMTL	Irradiated Materials Testing Laboratory
LAMDA	Low Activation Materials Development and Analysis
LD	localized deformation
LVDT	linear variable differential transformer
LWR	light water reactors
NBED	Nano beam electron diffraction
ORNL	Oak Ridge National Laboratory
PWR	pressurized water reactor
rdDF	Real-rod Dark-field
RIS	radiation induced segregation
SA	solution anneal
SAED	Selected area electron diffraction
SEM	scanning electron microscope
SS	stainless steel

STEM	scanning transmission electron microscopy
STEM-SI EDS	STEM spectrum imaging using EDS signals
STEM-SI EELS	STEM spectrum imaging using EELS signals
TEM	transmission electron microscope
TJ	triple junction
UM	University of Michigan
YS	yield strength

Toward an understanding of straining mode, grain boundary oxidation, and localized deformation on intergranular cracking of neutron irradiated austenitic stainless steels in pressurized water reactor relevant conditions

1. INTRODUCTION

The goal of this study is the determination of IASCC susceptibility of highly irradiated SA304 SS and CW316 SS in simulated PWR primary water with various damage levels (5.4 to 125.4 dpa), in particular, the determination of the stress to cause crack initiation, the correlation to microstructural features, and identification of any precursor state and potential mitigation strategies. The main interests are the dose dependence of crack initiation to very high dpa, the nature of the initiation site, the role of localized deformation and the grain boundary oxidation in crack initiation of highly irradiated austenitic stainless steel. The outcome of this program will provide a firmer understanding of parameters and microstructures governing IASCC and key elements that need to be included in a predictive model of the initiation of intergranular cracks that can be used to develop mitigation strategies [1]. IASCC continues to cause failures in key components of both PWRs and BWRs in the US and international reactor fleets. Identified in the 1960s, IASCC is generic in that all water reactors have exhibited susceptibility over a wide range of alloys and components. The problem will gain increasing importance in the coming years due to following two factors: 1) the life extension to 60 years and now to 80 years for the existing reactor fleet, and 2) the introduction of advanced reactors that will be subjected to the same types of environments. Therefore, understanding the mechanisms responsible for IASCC and establishing mitigation strategies are of high priority. Between the years 2000 and 2010, tensile and compact tension specimens as well as transmission electron microscope (TEM) discs of multiple alloys were irradiated in the BOR-60 fast reactor in RIAR, Russia as part of the framework of BORIS (BOR-60 Internal Study) irradiation experiments [2, 3]. The typical dose range was 5–20 dpa, but several capsules reached or exceeded 100 dpa. Irradiated specimens were involved in multiple programs including the Cooperative IASCC Research program [3]. Under certain circumstances, irradiated materials and untested specimens were made available to research teams working in the radiation materials field. Types 308, 304, and 316 stainless steel specimens with various dpa levels were among the samples irradiated in BOR-60.

During FY2016–2017, a collaborative effort was launched to transport several high- and very-high-dose specimens (up to 125 dpa) from Dimitrovgrad, Russia, to Halden, Norway, and after that to Oak Ridge National Laboratory (ORNL) in Oak Ridge, Tennessee. Much of the effort involved acquiring the proper license(s) and documenting that irradiated materials were appropriately prepared for shipment. The irradiated materials arrived in Halden, Norway, on August 23, 2016. After that, new activity calculations, inventory, additional packaging, documentation, and licensing efforts were pursued. The materials were shipped from the Halden reactor to ORNL in early 2018. In March 2018, 13 tensile specimens were

delivered to the Irradiated Materials Examination and Testing hot cell facility at ORNL. The internal holder with specimens was extracted and examined, revealing no transportation-related issues. Finally, specimens were unloaded and underwent individual examination and inventory and were made available to this project. This study utilizes several stainless-steel specimens (solution-annealed 304 SS and cold-worked 316 SS) that were irradiated in the BOR-60 liquid sodium fast reactor to doses ranging from 5.4 to 125.4 dpa.

In the last two decades, much progress has been made in understanding IASCC susceptibility, though a clear cause-and-effect has yet to be established on the mechanism of intergranular cracking in highly neutron irradiated stainless steels in the PWR environment. As reported in the previous LWRS program annual reports, to evaluate the IASCC susceptibility of these materials, a constant extension rate tensile test technique was used to reveal the change of fracture behavior and mechanical property with various dose levels. The current objective and experimental approach are basically to identify the role of various straining modes (single, interrupted, and constant load), and pre-oxidation in no-load condition and subsequent straining in an inert gas atmosphere, on intergranular cracking of neutron irradiated stainless steels. For this purpose, four-point bend tests were conducted to identify the critical stress to induce crack imitation and the microstructure features that correlate with crack initiation. An advantage of the bend test is that it creates a stress gradient through the sample thickness such that cracks grow into a progressively decreasing tensile stress, slowing crack propagation and preserving the sample beyond formation of the first crack. Furthermore, this test creates an area at the surface of nearly constant strain, enhancing the possibility of observing multiple crack initiation sties on a single specimen. Combined with the systematic test conditions (single straining, interrupted straining, constant load, and separation of oxidation and loading), surface conditions (GB oxidation, dislocation channels) were monitored up to and after intergranular cracking with the aim of providing a much clearer view of factors affecting the IG cracking.

2. EXPERIMENT

2.1 Materials and Specimens

2.1.1 Materials

The alloys investigated in this study are ~15% cold-worked (CW) 316 stainless steel (SS) and solution annealed (SA) 304 SS. The chemical compositions of the alloys in this program (in wt.%) are given in Table 1. The irradiations were performed in BOR-60 fast reactor at a temperature of 320°C with a neutron flux of ~1.8×10^{15} n/cm^{2}s (E>0.1 MeV), which corresponds to a damage rate of 9.4×10^{-7} dpa/s using the NRT model [2]. In the table, the suffix E stands for cold-worked material, and the suffix H represents the traditional solution annealed condition.

Table 1. Chemical compositions (wt.%) of the 300-series stainless steels.

Alloy/heat	C	S	P	Si	Mn	Ni	Cr	Mo	Cu	Co	Nb-Ta	B (ppm)	O (ppm)	N (ppm)
316-1 E/EDF	0.054	0.022	0.027	0.68	1.12	10.6	16.6	2.25	0.24	0.12	0.01	5	41	230
304-1 H/Creusot-Loire	0.022	0.0007	0.032	0.38	1.79	9.88	18.61	-	0.25	0.064	-	9	-	610

2.1.2 Specimen Preparation

Two pieces of material sliced from a tensile bar head using Electron Discharge Machining (EDM) were used to prepare four-point bend specimens. The position where the slices were made and the dimensions of the four-point bend specimen are shown in Figure 1. The remaining material was used to prepare transmission electron microscopy (TEM) specimens, to study the microstructure in the as-received irradiated condition. Rectangular samples with 1 mm thickness were made after EDM cutting. A Buehler Mini-met 1000™ sample grinding and polishing tool performed sample thinning to a target thickness of 800 μm using 120, 180, and 340 grit SiC grinding paper on each side to achieve a uniform thickness (final thickness variations were less than 10 μm). One side of the sample was then polished with a nylon pad containing 3 μm polishing media in the Mini-met™ and subsequently electrochemically polished in a Struers LectroPol-5™ system in four steps. One electrochemical polishing step was applied for 15 s at a potential of 30 V at 20 °C in a commercially available Struers A2 solution (60% perchloric acid). The final dimensions of the four-point bend sample are shown in Figure 1b. The ID, dose, and thickness of all samples used for this research project are given in Table 2.

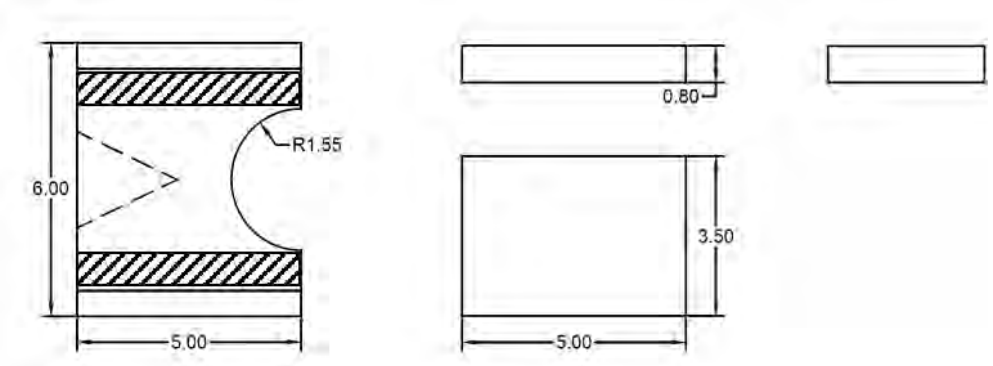

(a) (b)

Figure 1 Schematic showing (a) tensile bar head dimensions and location of the cut (the marked area), and b) bend test sample dimensions (unit: mm).

Table 2. High dose specimens used for this research project.

Alloy/heat	Parent tensile sample ID	Four-point bend sample ID	Dose (dpa)	Thickness (μm)
316-1 E	B98	B98-B1	42	820
316-1 E	B101	B101-B1	46.9	720-800
316-1 E	B103*	-	46.9	-
316-1 E	B89	B89-B1	67.4	800
316-1 E	B35	B35-B1**	125.4	830
304-1 H	A84	A84-1-1**	5.4	800
304-1 H	A84	A84-1-2	5.4	900
304-1 H	A98	A98-1-1	69	813
304-1 H	A98	A98-1-2	69	935
304-1 H	A98	A98-3	69	844
304-1 H	A96	A96-1-2	95	886
304-1 H	A96	A96-1-1	95	887
304-1 H	A32	A32-1-1	125.4	913

*FIB lift-outs were prepared from the CERT tensile sample for TEM analysis.

** FIB lift-outs were prepared from the tested bend samples for TEM analysis.

2.2 Test Systems and Procedures

2.2.1 Autoclave System

The four-point bend testing system IM2 is located in an irradiated material testing lab (IMTL) at UM. The water loop schematic diagram is shown in Figure 2. The water loop consists of two sub loops, loop 1 for conditioning the water at room temperature and low pressure, and loop 2 for simulating light water reactor environment at high temperature and high pressure. The environmental parameters such as conductivity and dissolved gas concentration are controlled in loop 1. The water is then pressurized and heated in loop 2, reaching the desired temperature and pressure in the autoclave and recirculated to the primary water column. The conductivity and dissolved oxygen (DO) are monitored at both inlet and outlet of loop 2.

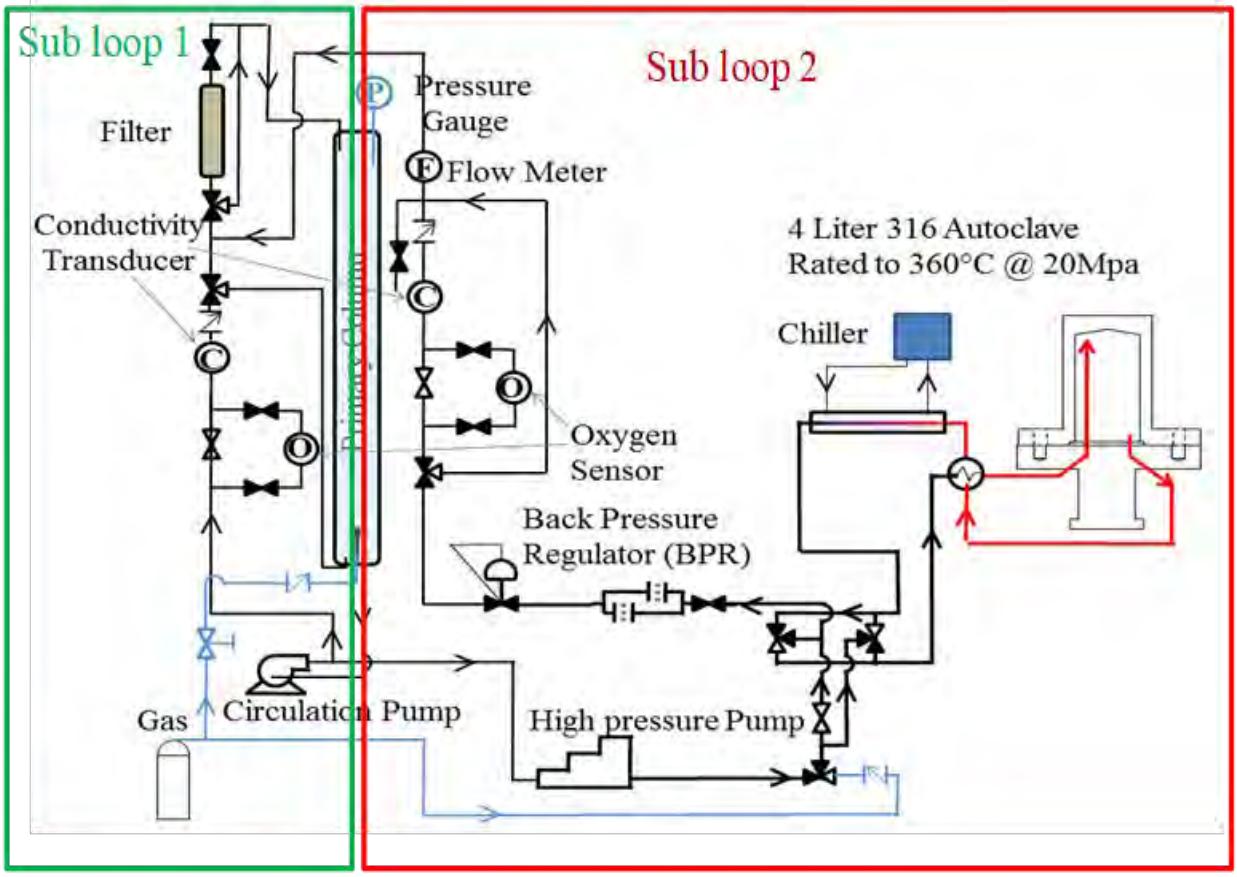

Figure 2. Schematic of the water loop used in the testing systems in the Irradiated Materials Testing Laboratory.

The IM2 loading system has one pull rod located right at the center of the autoclave head, which was used to meet the requirement of fine control of the deflection of the four-point bend specimen (see Figure 3). The application of load is using a 50 kN servo motor. A linear variable differential transformer (LVDT) is mounted on the pull rod to measure displacement. A load cell was connected with the pull rod, which was used to accurately measure the load applied to the sample. The pull rod is sealed at the feed-through into the autoclave with a self-energizing graphite seal with an internal spring that expands under pressure. The pull rod inside of the autoclave is connected to an Inconel 718 sample loading fixture. Electrical insulation is provided by zirconia washers located in the loading fixtures. After loading the specimens, the autoclave body is sealed to the autoclave head, thus preventing any leakage during the experiment.

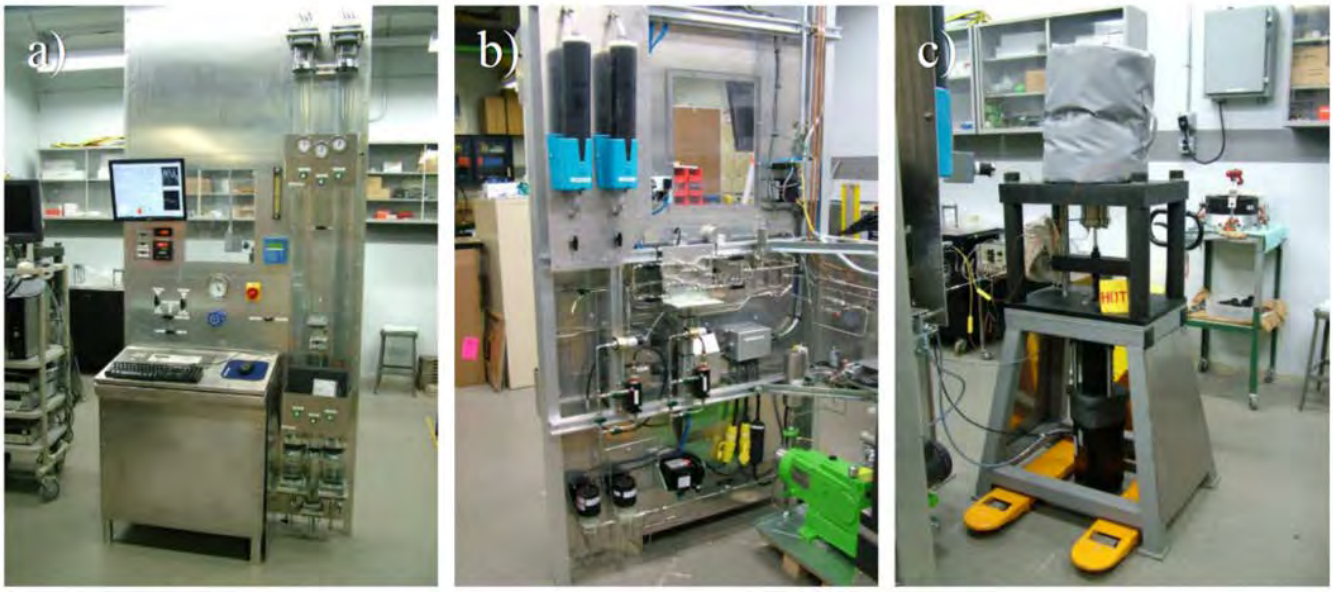

Figure 3. Images of the IM autoclave test system and water loop. a) Control panel front, b) control panel back with plumbing and sensors, and c) load frame, motor, and autoclave.

2.2.2 Four-Point Bend Testing Conditions

Testing environment and straining modes

The four-point bend tests were conducted in various modes of straining. The various modes of straining are constant strain rate, and constant load. Both of these straining modes were conducted in a simulated PWR primary water environment. The PWR primary water environmental parameters and the strain rate are summarized in Table 3.

Table 3. PWR primary water environmental parameters and strain rate for four-point bend tests.

Parameter	**PWR primary water**
Temperature (°C)	320
Pressure (MPa)	13.7 (2000 psi)
Inlet conductivity (µS/cm)	21.53
H_2 concentration (cc/kg)	35
O_2 concentration (ppb)	<5
Boron as H_3BO_3 (ppm)	1000
lithium LiOH (ppm)	2
pH at 25°C	6.5
Strain rate	4.3×10^{-8}/s
Load	Constant load at 98-100 lb

Fixture for the four-point bend sample

The four-point bend test method was developed by Stephenson as reported in reference [4] and the detailed description of this method can be found in reference [5]. The four-point bend sample has a constant strain area of 0.5 mm × 3.5 mm, which makes it possible to locate the crack initiation site in a reasonable time. The four-point bend test fixture used for this study was fabricated from Inconel 718 alloy in accordance with the schematic shown in Figure 4. Heat treatment of post-fabricated fixture parts created a hardened state to prevent deformation during bend testing. Four round posts called centering pins, elevated from the bottom support surface by 0.4 mm, surrounded the sample to prevent rotational misalignment. Set screws to the left and right of the sample and centered the sample laterally and were retracted after pre-loading the sample to prevent constraint during bending.

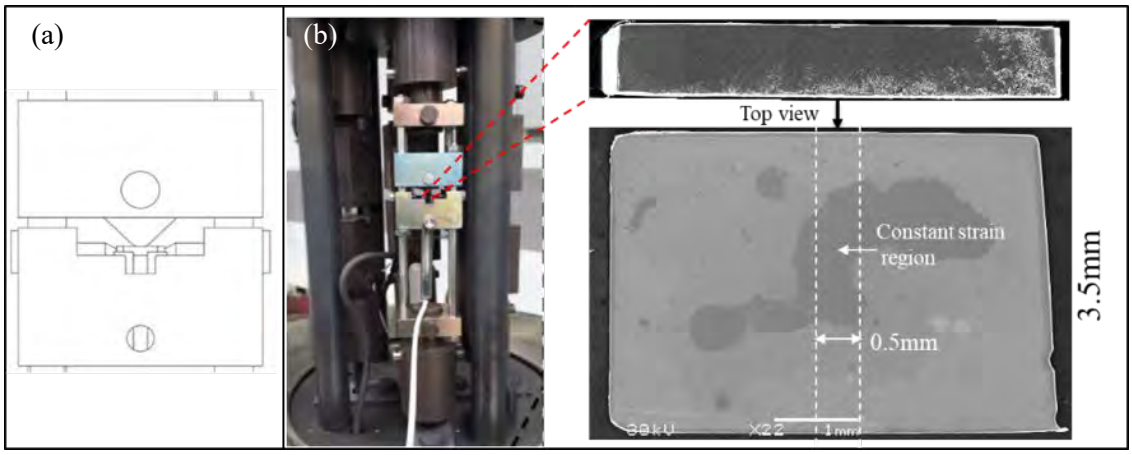

Figure 4. Schematic of the four-point bend loading fixture (a) and the real fixture including bend sample with side and top view (b).

System compliance at 320ºC in PWR primary water

For the high-temperature tests, direct sample deflection measurements were not possible in high-temperature environments due to limitations of the electronics in the device, therefore estimations of sample deflection were made by subtracting a load-dependent compliance correction factor from the crosshead deflection measurement. This compliance correction factor was determined in 320°C primary water by loading a ~10 mm thick 'bend' sample (hardened Inconel 718) with the same cross-sectional geometry as the actual bend test samples for multiple times. From our prior experience, it was observed that the applied loads for neutron-irradiated materials were significantly lower than 220 lbs. Therefore, the compliance measurements included the entire range of loads applicable to neutron-irradiated materials. Subtraction of the compliance from the measured crosshead LVDT displacement gives an approximation to the actual deflection at the sample surface. Due to its large thickness, it was assumed that no sample deflection occurred during loading, and compliance correction curves were determined by fitting a cubic polynomial to the resulting load vs. crosshead displacement curves, as shown in Figure 5. Compliance correction curve determination was repeated twice for accuracy and averaged to determine the following correction factors in 320°C primary water:

$$CF_{PW} = 2.03931 \times 10^{-5} P^3 - 0.01072 \times 10^{-5} P^2 + 3.39312P - 165.28 \quad (1)$$

where P is the applied load in N and CF_{PW} is the correction factor in the PWR environment in μm.

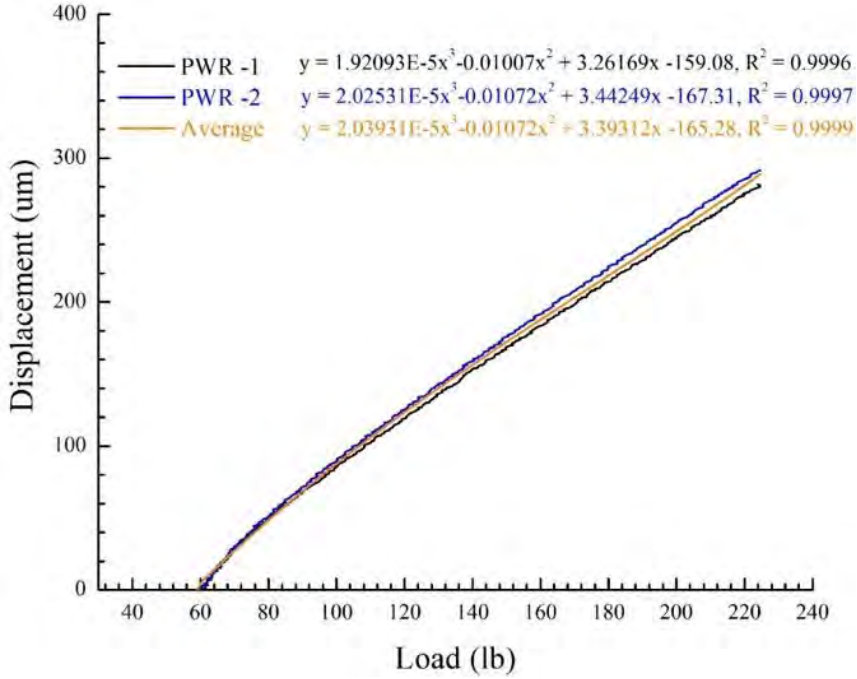

Figure 5. Compliance measurements for the four-point bend test in single specimen configuration in PWR. The averaged curve was used in our program to calculate the displacement of bend sample.

2.2.3 Constant Strain Rate Bend Tests

All bend tests were carried out using the IM2 autoclave system in IMTL at UM. Bend samples were loaded on the fixture with a tailor-made tweezer, centered by tightening the set screws on either side uniformly and held in place by bringing the loading points into contact with the sample and lightly tightening the connection of the pull rod at the system crosshead. Sample bending was performed by moving the crosshead at a constant rate of 1.714 x 10^{-8} in/s, generating a constant strain rate of 4.3 x10^{-8} s^{-1} on the polished surface, until achieving the desired amount of load. The target stress in the constant strain region was achieved by applying a corresponding load based on the linear behavior of stress with load, as shown in Figure 6. The relationship between the bend yield load in four-point bend and the tensile yield stress was formed utilizing previous experimental data on neutron-irradiated 304 stainless steel specimens by Kale Stephenson et al. [4, 5] and benchmarking experiments utilizing a heat of 316 SS cold-worked to varying degrees. While there is some variability, this comparison allowed a prediction of the bend yield load based on previous measurements of the tensile yield stress. Due to the linear relationship, it was assumed that loading to a percentage of the bending yield load in a four-point experiment is directly comparable to loading to that percentage of the yield stress for the specimen.

There is a tare load applied to the bend specimen by the vessel water pressure that is not directly measured by the pull rod load cell. With a 4.76 mm diameter pull rod and the 2000 psi system pressure, a tare load of 55.4 lb (246.5 N) was added to the bend specimen, under simulated PWR conditions. The testing was performed in increments to create crack initiation and limit the amount of crack propagation in

the material. Increments are reported in this report as the fraction of irradiated yield stress. This interrupted straining procedure needs to be conducted only when the crack is not initiated at the first desired load. In these constant strain rate mode tests (single as well as interrupted straining), the unloading (i.e. get rid of the load applied on the sample) has been done very quickly (with 1000x higher actuator rate).

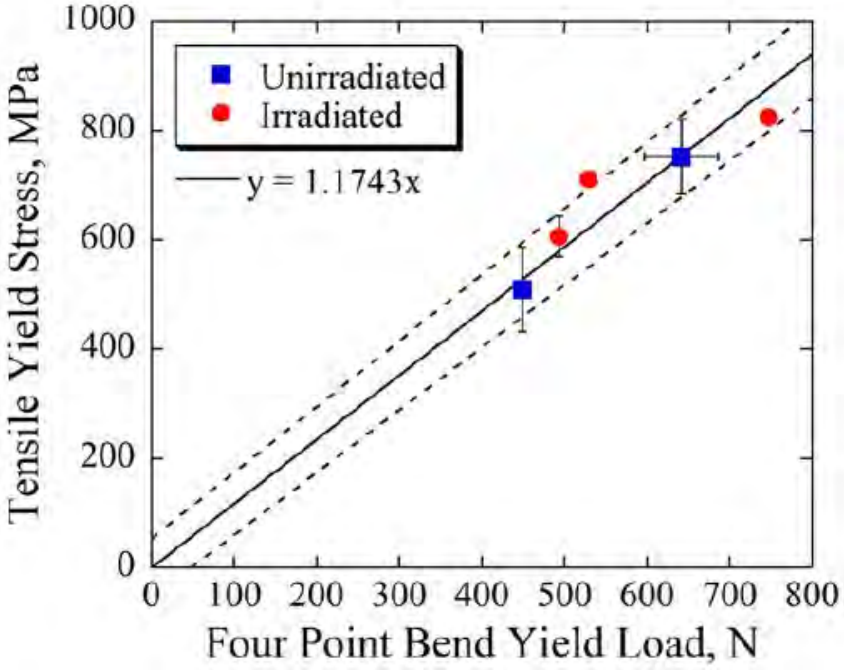

Figure 6. Comparison between the measured tensile yield stress and four-point bend yield load for several specimens, both irradiated and unirradiated. The linear fit was utilized to predict the bend yield load for conditions previously strained in tensile experiments.

The relationship between bend yield load and tensile yield stress was obtained from specimens with a thickness of ~800 µm. In a four-point bend experiment the maximum bend stress, σ_{max}, is directly related to the specimen thickness. The maximum stress in the tensile surface is inversely proportional to the square of the thickness [6], as described by the following equation.

$$\sigma_{max} \propto \frac{1}{h^2} \quad (2)$$

Therefore, the applied load was adjusted based on the thickness of the sample when a certain fraction of yield stress was targeted.

2.2.4 Constant Load Bend Tests

In single and interrupted straining four-point bend tests, the unloading (i.e. dropping the load applied on the sample) has been done very quickly upon reaching the desired amount of load. The constant load test was conducted by keeping the sample at the targeted stress for 200 h after achieving the desired amount of load in a simulated PWR primary water environment. To reach the target stress, slightly increased strain rate (4.3×10^{-7} s^{-1}) was used. Upon reaching the desired amount of time (i.e. 200 h) by holding the sample in a targeted stress level, the unloading was done very quickly as stated above for the single and interrupted straining tests. In constant load mode also, the testing was performed in increments to create crack initiation

when there was no cracking at the first desired amount of load itself, i.e. an interrupted constant load four-point bend test.

2.2.5 Pre-Oxidation in High Temperature Water

To prove that the initiation of an intergranular crack is possible only after the oxidation of grain boundaries exposed to high temperature water, a pre-oxidation step without application of load was conducted for a period of 210 h at 320 ℃ in simulated PWR primary water. Thereafter, the pre-oxidized specimen was strained in an inert argon gas atmosphere to assess the propensity for crack nucleation, i.e. rupturing of the oxidized grain boundary during straining in argon. Success in causing grain boundary fracture would establish that it is the oxidation of the grain boundary that is responsible for IG crack initiation.

2.2.6 Four-Point Bend Test in Argon

To avoid the corrosive environmental effect, i.e. to avoid the influence of simultaneous application of corrosion and stress, four-point bend tests were carried out in an inert argon gas atmosphere. Thus, straining in argon gas environment aimed to clarify the environmental contribution on intergranular cracking. The argon four-point bend tests were performed at 320℃ to be consistent with tests conducted in water. Though ultra-high purity argon was used, it was further purified to remove any trace amounts of water and oxygen from the system that could potentially oxidize the samples during straining. The autoclave test system was thoroughly purged for 12 h with the purified argon gas with a flow rate of 215 ml/min. To mimic the tare load condition (approximately, 55 lb) that the sample experiences in high temperature water, an initial strain rate of 4.3 $\times 10^{-5}$/s was used. Once the tare load condition is reached, the strain rate was switched to a typical constant strain rate of 4.3 $\times 10^{-8}$/s. As the sample was strained in well-purified flowing argon gas atmosphere, the environmental contribution to cracking was avoided.

2.3 Cracking Analysis

2.3.1 Crack Initiation Detection

After completion of each four-point bend test, the uniform strain area (0.5mm×3.5mm) of a tested sample was examined in SEM (JEOL JSM-6480) to determine the surface morphology and cracking susceptibility. As described previously, the bending experiments were conducted in small increments to more precisely identify points of crack initiation and study the microstructure responsible for crack initiation. After each stress increment, the specimen was removed from the autoclave and was examined in SEM. The uniform-strain region was imaged under 1000X magnification in BSE mode to record any sites of crack initiation as well as changes in the localized deformation. The GBs that are darker and wider than the others in BSE mode is most likely to change into cracks in the next strain test. Therefore, as much as possible GBs with that kind of features were traced after each stress increment to record the change in GBs and its surroundings. Then, the evolution of cracks and the microstructures that are responsible for crack initiation can be determined. The higher magnification SE- and BSE-images (5000X to 25000X)) were taken when the crack initiation was observed. The cracks and microstructure features at the crack initiation sites were characterized and their relationship with cracking was analyzed.

2.3.2 Cracking Standard Establishment

Definition of cracking

Crack initiation is a concept that is difficult to define and varies in different conditions. The scientific definition is that it is the formation of a mechanically distinct geometry that will tend to grow in preference to its surroundings. However, practically, it is the detectability that is likely to be achieved in-situ for a laboratory autoclave experiment. Also, as reported in reference [7], the width of an IG crack tip is less than 5 nm, indicating that crack width could be very small when cracking occurs. Therefore, to detect the crack with our available SEM and determine the correlation of microstructures with crack initiation, a standard for the cracking of GB must be established.

Figure 7a shows a crack from the tensile sample B89. It is well accepted that this is a crack as we can see the grain facet clearly down the crack. One common feature shared by all the cracks is that the crack is bounded by two bright lines which are believed to be the edges of the crack, and are created by the effect of the sharp curvature of the edges on the secondary electron (SE) production. The plot of gray value across the crack is given in Figure 7b, which was processed using ImageJ® software. The two peaks correspond to the two bright edges. Therefore, it suggests that the GB has cracked when two bright edges along the GB were observed in the SE image. Henceforth, this standard will be used to determine whether the GB is cracked.

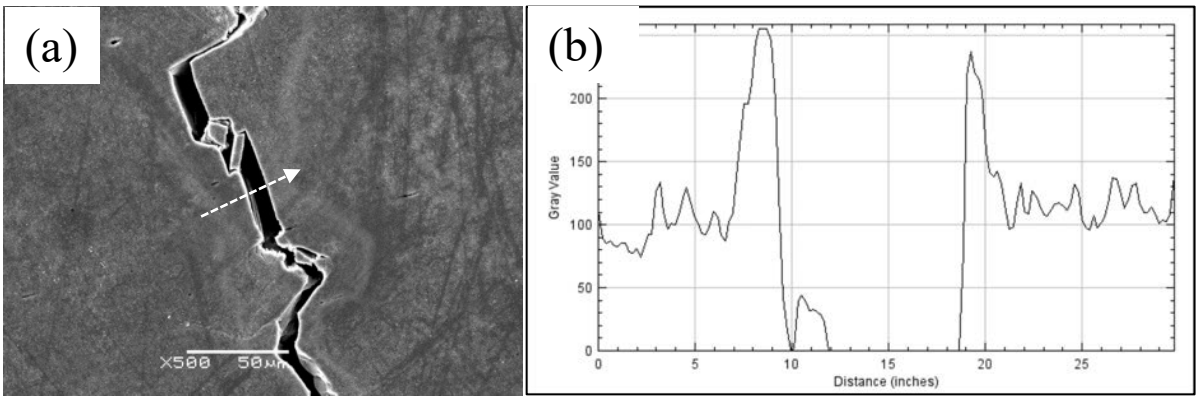

Figure 7. A well-defined crack from the tensile sample B89 (a) and the gray value plot taken at the dashed line (b).

State of GBs after exposure to high temperature water

Four GB states were observed after exposure to high-temperature water: intact, oxidized, suspected crack, and cracked, and are differentiated by the shape of the gray plot. As shown in Figures 8a & b, the intact GB is barely visible in the SE image and the gray value over it is irregular and noisy. However, the GB is clearer after oxidization, and gray value is less noisy, showing a "V" shape, Figures 8c & d. Figures 8e & f show a suspected crack and the gray value along the dashed line. There is only one bright line along with the GB and accordingly only one peak in the gray value plot. Though it looks like a crack it does not meet the cracking criterion we established. Hence, the GB meets this condition will be treated as a suspected crack. Figures 8g & h show a crack and the gray value along the dashed line. Two bright lines can be seen in the SE image as well as two peaks in the gray value plot. The distance of peak-to-peak is defined as the

width of the crack. For example, the width of the crack shown in figure 8g is ~100 nm. For now, the cracking standard has been established and will be used in this study. The image used to determine the state of the GB was taken at 15000x. This is the maximum magnification that our SEM equipment can go without compromising too much of the resolution.

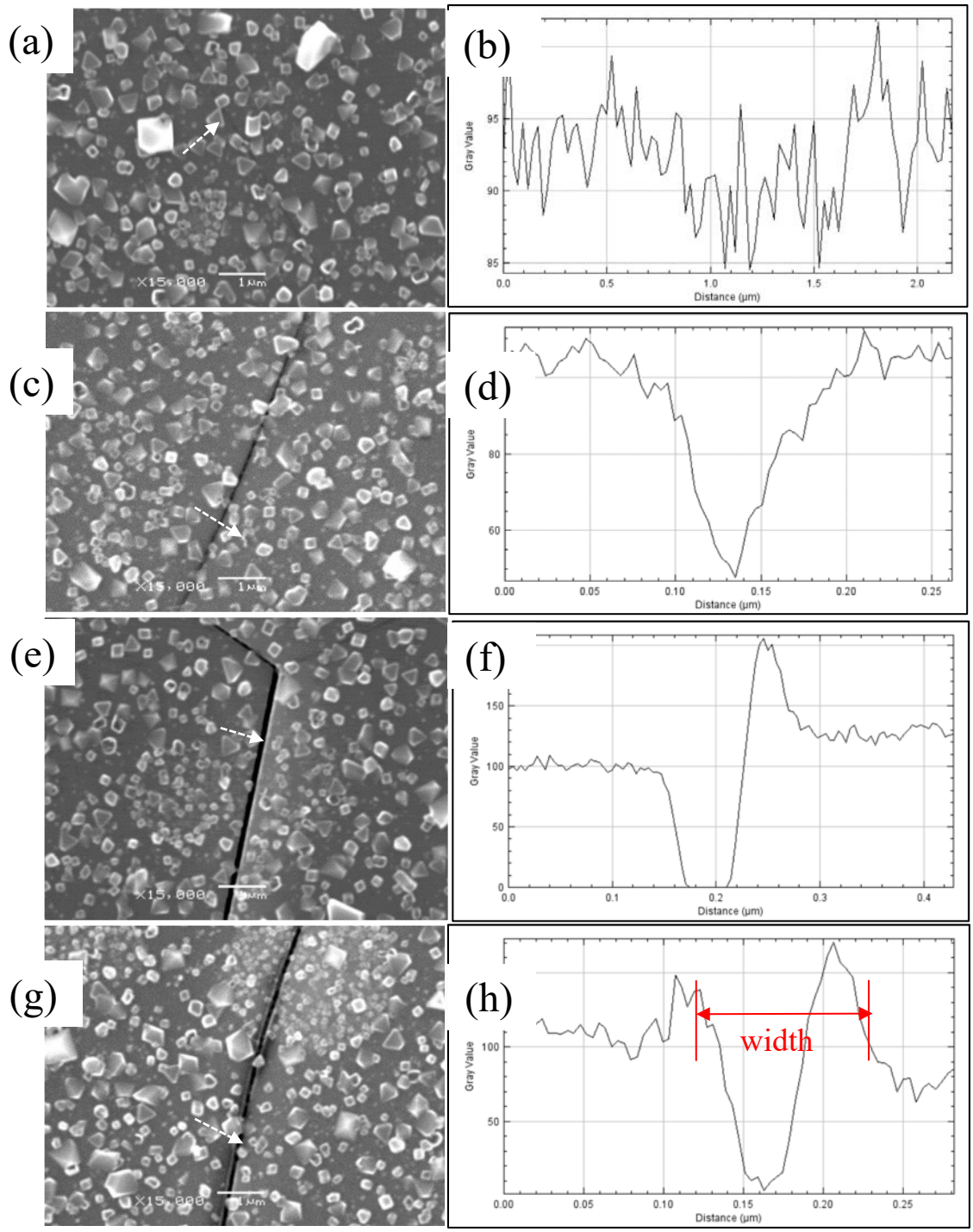

Figure 8. Intact GB after exposure to high-temperature water (a) and the gray value (b), an oxidized GB (c) and the gray value (d), a suspect crack (e) and the gray value (f), a small crack (g) and the gray value (h).

2.4 Microstructure and Microchemistry Characterizations by TEM

Focused ion beam (FIB) lift-outs for TEM study were prepared from the as-irradiated CERT sample B103 (CW316 SS; 46.9 dpa) and the four-point bend tested samples A84-1-1 (SA304 SS; 5.4 dpa) and B35-B1(CW316 SS; 125.4 dpa). The lift-outs were first cut and transferred to FIB grids with thickness of ~1.5 um at 30 keV at LAMDA facility in ORNL using a FEI Versa FIB-SEM. The lift-outs were further thinned at the Michigan Center for Materials Characterization (MC^2) at the UM using a Thermo-Fisher Helios 650 Xe Plasma FIB-SEM at 30 keV down to about 150nm and were finally thinned at 5 keV to reduce FIB damages induced at high beam energy. The final thickness of the TEM foils for B103 sample was about 80nm measured using electron energy loss spectroscopy (EELS) in a JEOL JEM-3100R05 TEM/STEM at MC2. The uncertainty in thickness measurements is typically 10% [8]. Frank loops were imaged using a Rel-rod dark-field (rdDF) technique with g = 1/2{311} [9] in a Thermo-Fisher Tecnai G2 F30 TWIN TEM. The number of loops from such a DF image (1024 pixels x1024 pixels) were counted using Gatan DigitalMicrograph software from which the total loop number was obtained by multiplying a factor 2 of the counted number. The sizes of the loops were measured from such a DF image with size smaller than 4 nm excluded, which has no more than 10% portion of the total loops features, as it was difficult to separate them from the precipitates or FIB damages/redepositions. Precipitates and grain boundary microstructures and microchemistry were characterized using the JEOL JEM-3100R05 TEM/STEM and a Thermo-Fisher Talos F200 at MC2 with both operated in STEM mode. The Talos is equipped with four $30mm^2$ SDD EDS detectors that can give strong X-ray signals for STEM spectrum imaging using X-ray signals (STEM-SI EDS) and thus was used for imaging precipitates and radiation induced segregations (RIS) at grain boundaries (GBs) for the B103 sample. The size and density of the precipitates were measured from EDS element maps using ImageJ, which display all the precipitates. The JEM-3100R05 equipped with double-aberration correctors and a Gatan Quantum 965 ER GIF system was used for grain boundary microstructures and microchemistry characterizations for the two bend samples (A84-1-1 and B35-B1) using HAADF STEM-imaging and STEM-SI based on X-ray signals and EELS signals (STEM-SI EDS and STEM-SI EELS) respectively).

3. RESULTS

3.1. Microstructure of CW316 SS (46.9, 67.4, and 125.4 dpa)

The microstructures of neutron irradiated CW316 SS (with dose level: 67.4 dpa and 125.4 dpa) samples have already been documented [1, 10]. In the present report, we present the microstructure data from the 46.9 dpa (B103) sample together with those from the 67.4 and 125.4 dpa samples for comparison. In all the three samples, we did not see any cavities. Thus, characterizations of those samples were focused on dislocation loops (faulted Frank loops), precipitates and RIS at grain boundaries.

3.1.1 Dislocation Loops

TEM rel-rod dark field (rdDF) images of dislocation loops in the three samples are shown in Figure 9. The rdDF images in Figures 9(b)-(d) were taken using the ½{311} diffraction circled by a yellow circle in Figure 9a which is a selected area electron diffraction (SAED) at an approximately {311} two beam

condition. These rdDF images show only half of all the loops in each sample. Table 4 shows that the average loop size is 8.8 nm, 9.2 nm and 8.5 nm for the 46.9 dpa, 67.4 dpa and 125.4 dpa samples, respectively. The measured number densities are 9.8 × $10^{21}/m^3$, 1.1 × $10^{22}/m^3$, 9.9 × $10^{21}/m^3$, respectively for the three samples. The results show that there is no significant difference in loop size and density among the three samples with much different damage levels. The size distributions of the loop in the three samples are shown in Figure 10, which are also similar. In the SAED pattern in Figure 9a, there is a weak ring feature corresponding to ~0.25nm that matches the {110} d-spacing of the $\gamma' - Ni_3Si$ phase, a common phase found in such alloys [11].

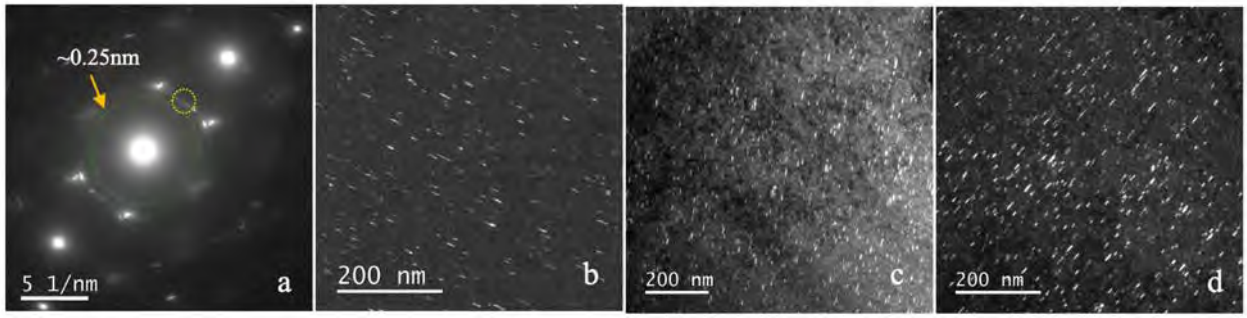

Figure 9. a) SAED pattern taken from B103 (CW 316 SS; 46.9 dpa) sample under a {311} two beam condition; rdDF TEM images (using g = 1/2{311}) showing the faulted dislocation loops in CW316 SS irradiated by neutron at dose levels of b) 46.9 dpa, c) 67.4 dpa and d) 125.4 dpa, respectively.

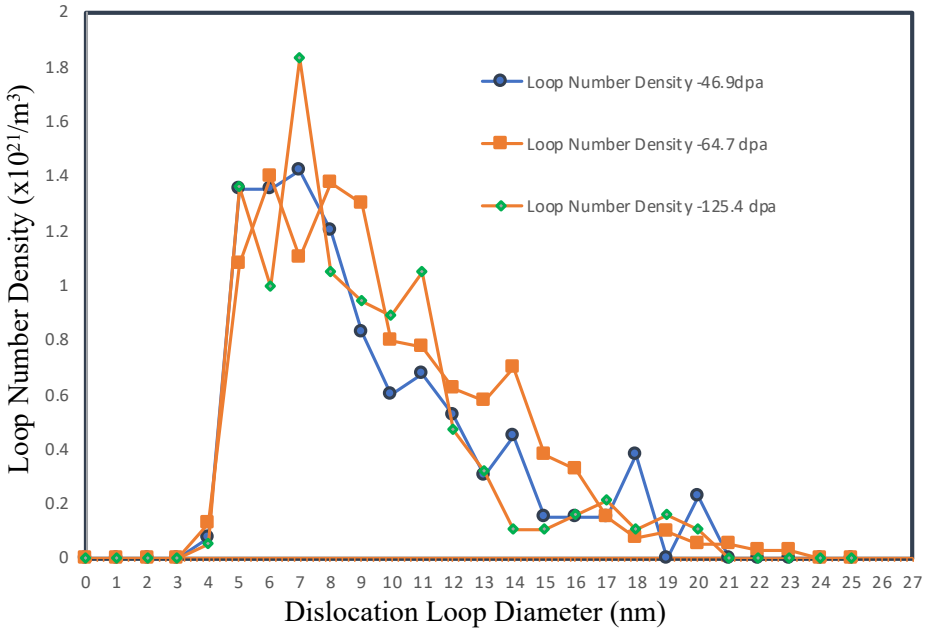

Figure 10. Size distributions of the loops in CW316 SS samples irradiated by neutron at dose levels of a) 46.9 dpa, b) 67.4 dpa and c) 125.4 dpa, respectively.

Table 4. Dislocation loop size and number density in CW316 SS samples with different dpa.

Dose (dpa)	Loop density (x10^{21}/m^3)	Loop diameter (nm)
46.9	9.8	8.8±3.8
67.4	11.0	9.2±3.7
125.4	9.9	8.5±3.5

3.1.2. Precipitates

According to SAED pattern shown in Fig. 9a, the precipitates in the three CW316 SS samples (46.9, 67.4, and 125.4 dpa) were found to be a Ni-Si rich phase, i.e. $\gamma' - Ni_3Si$. As a conventional TEM DF image obtained by using an objective aperture to select diffractions of a ring cannot display all precipitates. The sizes and distributions, of those precipitates were measured from Ni-maps collected by STEM-SI EDS as shown in Figure 11. As shown in Table 5, the measured size of the precipitates is, 6.9 nm, 6.3 nm, and 8.4 nm, and the density is 3.4 x10^{22}/m^3, 3.8 x10^{22}/m^3 and 4.5 x10^{22}/m^3 for the 46.9 dpa, 64.7 dpa and 125.4 dpa, respectively. The data from the 67.4 dpa and 125.4 dpa samples presented are different from our previous report in which the precipitates were characterized by TEM DF images which cannot show all the precipitates in a single image. The size distributions of the dislocation loops in the three samples are shown in Figure 12. No significant differences in both the size, size distribution and density of the precipitates were seen in the three samples. The highest dose sample has a slightly higher density over the two lower dose samples.

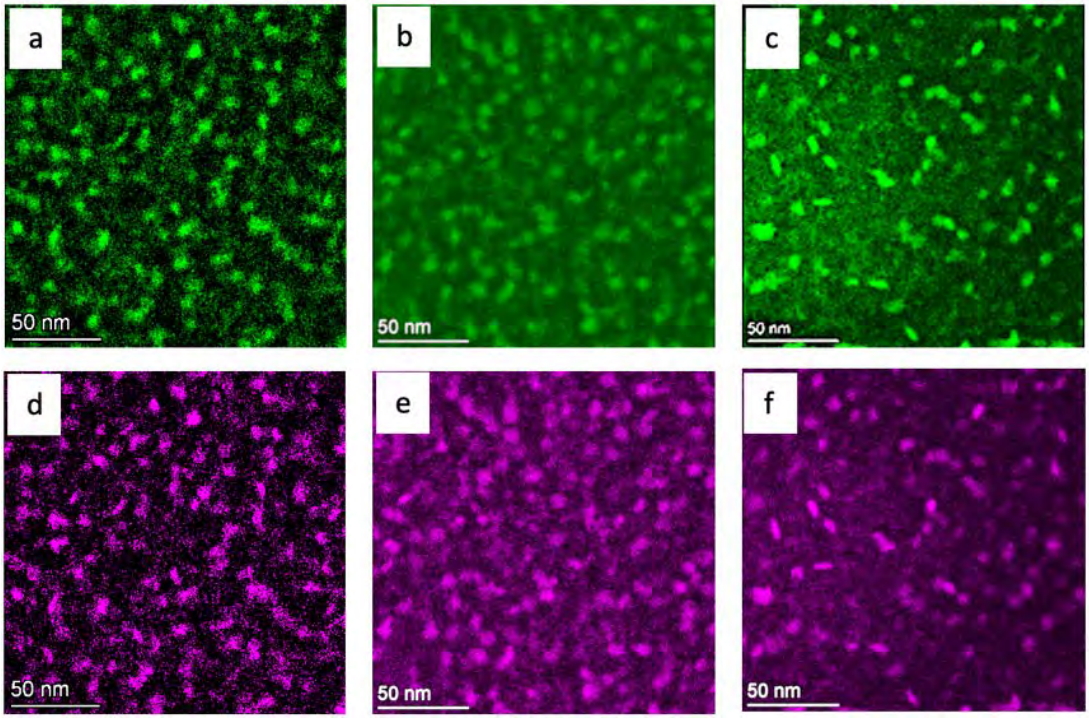

Figure 11. Ni-maps (a-c) and Si-maps (d-f) collected from the CW316 SS irradiated by neutron at dose levels of a-d: 46.9 dpa, b-e: 67.4 dpa and c-f: 125.4 dpa, respectively.

Table 5. Precipitate size and number density in in CW316 SS samples with different dpa.

Dose (dpa)	Precipitate density (x10^{22}/m^3)	Precipitate size (nm)
46.9	3.4	6.9±1.8
67.4	3.8	6.3±1.6
125.4	4.5	8.4±2.3

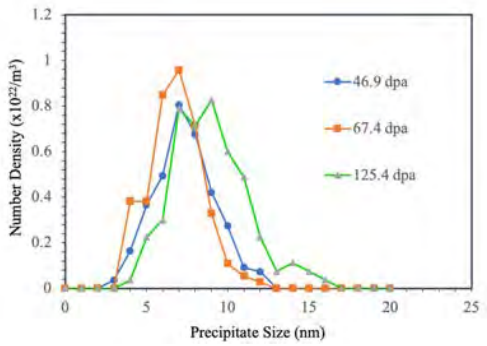

Figure 12. Size distributions of the precipitates in CW 316 SS samples irradiated by neutron at dose of a) 46.9 dpa, b) 67.4 dpa and c) 125.4 dpa, respectively.

3.1.3. Radiation induced segregation (RIS)

Figure 13 displays STEM-SI EDS data showing the distributions of Cr, Fe, Ni, and Si at the high-angle grain boundaries (HAGBs) in the CW316 SS 46.9 dpa, 67.4 dpa and 125.4 dpa samples, respectively. It should be mentioned that only isolated Ni-Si rich particles were formed at the twinned boundaries much like the Ni-Si rich phases formed inside the grains (see the maps from the 67.4 dpa sample). So even the three samples have many twinned boundaries, more focuses were paid to the HAGBs. Results show that a continuous layer enriched in Ni and Si while deficit in Cr and Fe are formed at the HAGBs in the three samples. In Figures 15a, 5f and 5k, yellow arrows (the purple frames highlight the width of the lines) across the GBs were drew along which element profiles across the GBs were extracted as shown in Figure 14.

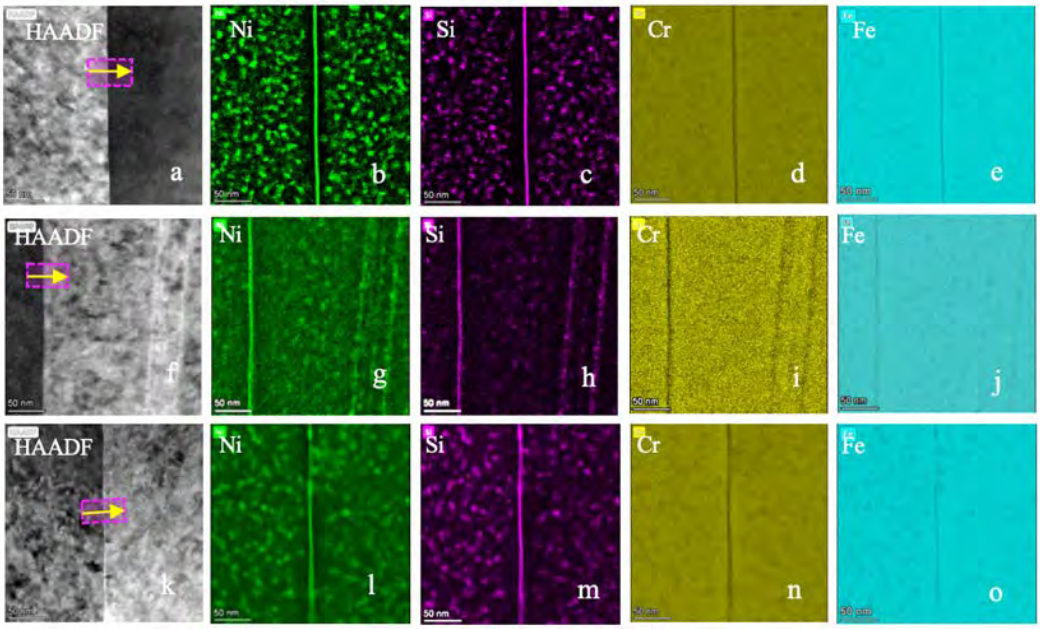

Figure 13. HAADF images (a, f, and k), Ni-maps (b, g and l), Si-maps (c, h and m), Cr-maps (d, i and n) and Fe-maps (e, j and o), collected from CW 316 SS samples irradiated by neutron at dose of a) 46.9 dpa, b) 67.4 dpa and c) 125.4 dpa, respectively.

To compare the RIS degree in the three samples, quantified element profiles (in wt.%) of Ni, Si, Cr and Fe across the GBs outlined in figure 13 a, f and k are plotted in figure 14. Figure 14 a-c show Ni-, Si-, Cr- and Fe-profiles collected from the 46.9 dpa, 67.4 dpa and 125.4 dpa samples, respectively. The composition of the GBs was measured from the points at the GBs with the strongest Ni signals for each sample shown in Table 6. Results show that the lowest dose (46.9 dpa) sample has more Ni while the highest dose (125.4 dpa) sample has more Si at the GBs.

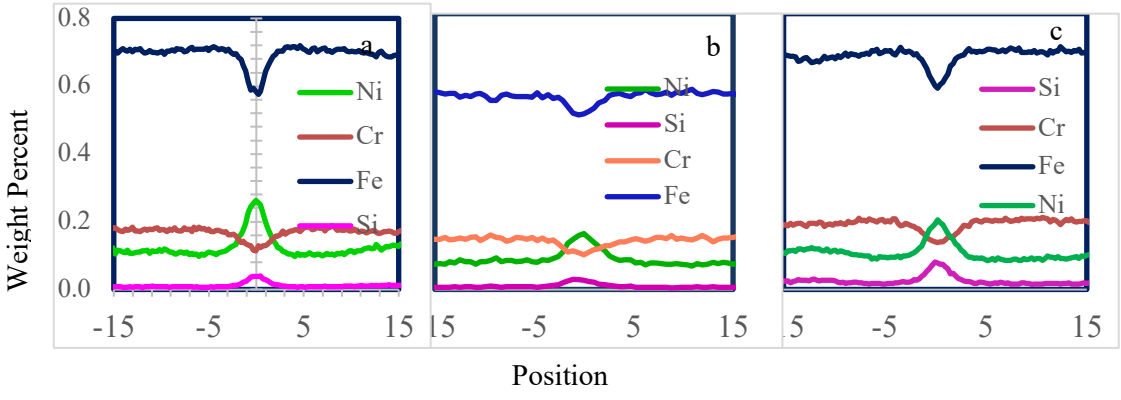

Figure 14. Element profiles across the GBs in CW 316 SS irradiated by neutron at dose levels of (a) 46.9 dpa, (b) 67.4 dpa and (c) 125.4 dpa, along the arrow lines in Figure 13 a, f, and k, respectively. The centers of the GBs were assigned at which the Ni signals are highest in each sample.

Table 6. Composition of the GBs in CW 316 SS samples irradiated by neutron at dose levels 46.9 dpa, 67.4 dpa and 125.4 dpa shown in Figures 13 and 14.

Dose	Ni (wt.%)@GB	Si (wt.%)@GB	Cr (wt.%)@GB	Fe (wt.%)@GB
46.9 dpa	26.3	3.9	11.4	58.4
67.4 dpa	20.3	3.4	12.6	63.7
125.4 dpa	20.2	7.8	13.6	58.4

3.2. Constant Strain Rate Four-Point Bend Test

The results of the four-point bend test conducted at a constant strain rate on the CW316 SS sample is presented in this section. The bend load versus LVDT displacement curves as well as the detailed SEM examination of the uniform strained region upon completion of the bend test are presented. Also, the cracks that initiated in the uniform strained region upon straining at constant strain rate were characterized and quantified.

3.2.1. Bend Test Results of CW316 SS (42 dpa)

This CW316 SS B98-B1 (42 dpa) sample was strained to 0.5YS at a constant strain rate in a simulated PWR primary water environment. The irradiated yield strength of the CW316 SS samples (obtained from the CERT tests) with the various dose level (up to 125.4 dpa) showed very similar values, i.e. 1020-1024 MPa. The 0.5YS was converted to a bend yield load through the linear fitting of the relationship between tensile yield stress and the four-point bend yield load, as explained in the experimental section. The targeted bend load was applied to a four-point bend sample by the controlling the crosshead moving at a constant rate of 1×10^{-6} s^{-1}. Upon reaching the targeted load (i.e. 0.5YS), the crosshead immediately reversed its direction of movement and returned to the initial set point.

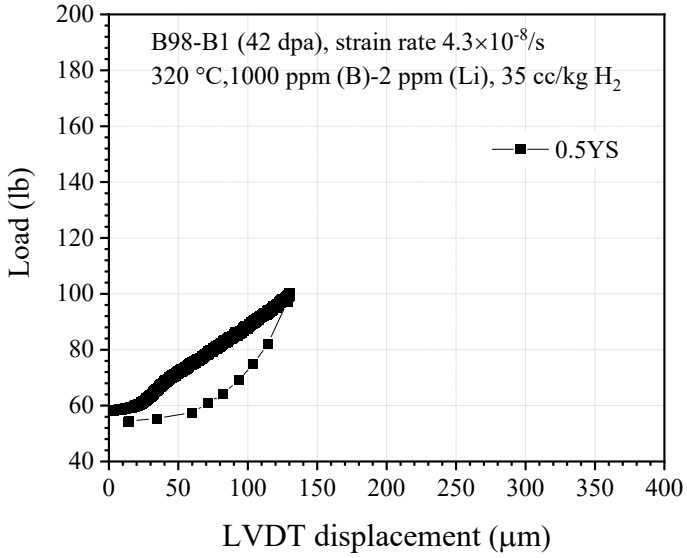

Figure 15. The bend load vs. the LVDT displacement for the sample B98-B1 (CW316 SS; 42 dpa) strained to 0.5YS at a constant strain rate of 4.3 $x10^{-8}$ s^{-1}. Cracks were observed at this straining condition.

Figure 15 presents the bend load versus the LVDT (crosshead) displacement curve for the B98-B1 (CW316 SS; 42 dpa) sample strained to 0.5YS at a constant strain rate of 4.3×10^{-8} s^{-1}. Tare load imposed by the PWR primary water environment was also added when this load vs. LVDT displacement curve was plotted. From this plot, the applied load to achieve the targeted stress is known. Also, the increase of LVDT displacement with increase of load clearly demonstrates a linear relationship. Upon completion of this constant strain rate bend test, the sample was then characterized in the SEM. As several cracks were observed after straining to 0.5YS, no further bend test was carried out on this sample.

The results obtained from the interrupted straining four-point bend tests at constant strain rate in a simulated PWR primary water environment, for the CW316 SS samples with various dose levels (46.9, 67.4 and 125. 4 dpa) were already documented [1, 10]. Table 7 presents the summarized results of the straining history and the crack initiation stress for the CW316 SS samples with the range of dose levels up to 125.4 dpa.

Table 7. The crack initiation stress for the CW316 SS samples with various dose levels.

Sample ID	Dose (dpa)	Constant strain rate bend test history (YS)	Initiation stress (YS)
B98-B1	42	Single strain: 0.5	0.5
B101-B1	46.9	Interrupted straining: 0.4, 0.6, 0.8	0.6
B89-B1	67.4	Interrupted straining: 0.4, 0.5, 0.6	0.5
B35-B1	125.4	Interrupted straining: 0.4, 0.45, 0.5, 0.6	0.45

3.2.2. Oxidation and Cracking Characteristics

Upon completion of the four-point bend test, the morphology of the oxidized and cracked sites in the uniform strain region of B98-B1 (CW316 SS; 42 dpa) sample were characterized using SEM. Prior to the bend test, the sample surface was examined in SEM, and inclusions were observed on a few places on the surface, probably as a result of alloy processing.

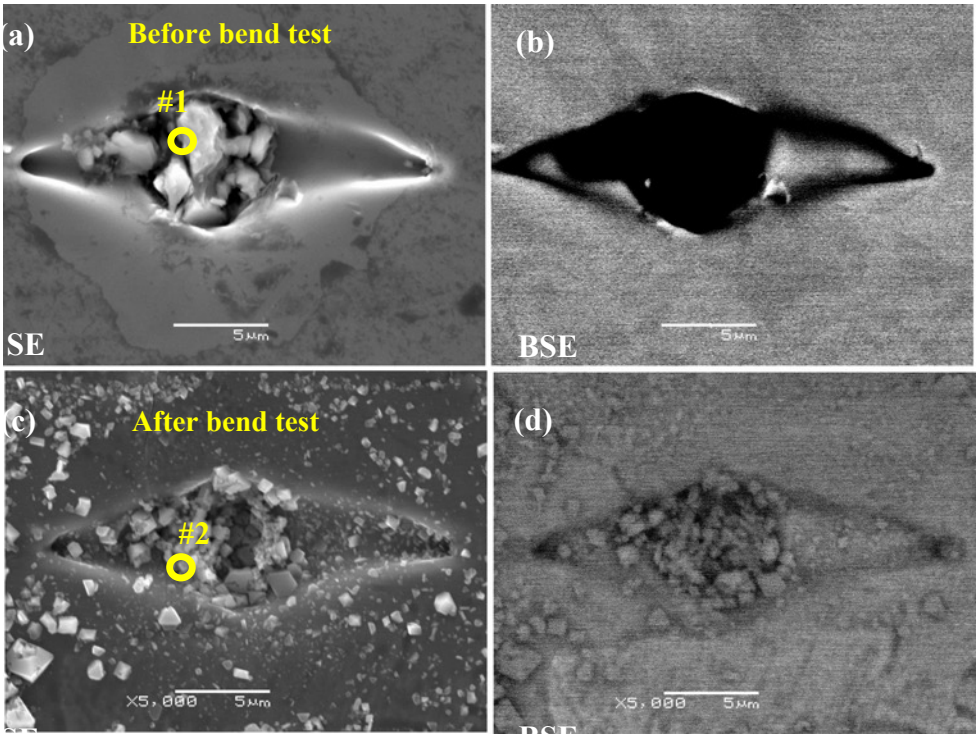

Figure 16. The SE and BSE images of the morphology of the oxide inclusion site observed in B98-B1 (CW316 SS; 42 dpa) sample before (a-b) and after (c-d) the four-point bend test in PWR primary water environment. No cracks initiated at the inclusion site. The yellow-circles are the EDS spot analysis location, see Table 8 for the quantitative results.

Figure 16 illustrates the SE and BSE images of surface morphology of the inclusion site captured before and after the bend test, in the uniform strain region. As shown in Figure 16a and 16b, these inclusions are a few μm in size and irregular in shape. The composition of the inclusions was characterized using EDS, and the results are presented in Table 8 which shows that the inclusions are a mixture of Al, Ca, Mg and some amount of Si oxides. The same inclusion site was imaged after a bend test (see figure 16c and 16d), to check whether the inclusion had any influence on cracking. The inclusion site did not experience any significant changes in appearance, and no cracking was observed as well, only Fe-rich oxide crystallites were re-deposited from the exposed PWR primary water environment.

Table 8. EDS-quantitative analysis of the oxide inclusion site for the sample B98-B1 (CW316 SS; 42 dpa) examined before and after bend test.

Element	EDS spot #1		EDS spot #2	
	Wt.%	At.%	Wt.%	At.%
O	42.41	59.10	24.58	53.10
Mg	1.76	1.62	-	-
Al	25.21	20.84	-	-
Si	7.82	6.21	-	-
Ca	19.80	11.02	-	-
Cr	0.81	0.35	10.81	7.18
Fe	2.18	0.87	55.57	34.39
Ni	-	-	9.04	5.32

It has been reported that MnS inclusions on the irradiated 304L alloy, dissolves in a simulated normal water chemistry condition and form oxide caps and create crevice condition with a high propensity for crack initiation [4]. However, this was not the case with this CW316 SS (42 dpa) sample. As can be seen in figure 16c, the observed oxide inclusion (shown in figure 16a) appears to have either fallen out or was washed away in the high temperature water exposure condition.

The SE-micrographs obtained from the cracked and oxidized GBs were stitched together to show the cracking behavior of the B98-B1 (CW316 SS; 42 dpa) sample upon straining to 0.5YS in a four-point bend test in PWR primary water environment. Figure 17 presents the typical cracking characteristics of sample B98-B1. As can be seen in Figure 17a, the oxidized grain boundary is dark in color and quite visible in this stitched 15000x SE micrograph. Moreover, it clearly reveals that the oxidized grain boundary is fractured, as per the established cracking criteria discussed in the experimental procedures section. The gray value plot across the fractured boundary (see Figure 17b) has two peaks which correspond to the separated edges of the adjacent grains confirming the existence of a crack. The noisy gray value plot obtained from the unfractured part of the oxidized grain boundary (see Figure 17c) indicates no cracking at this portion of the GB.

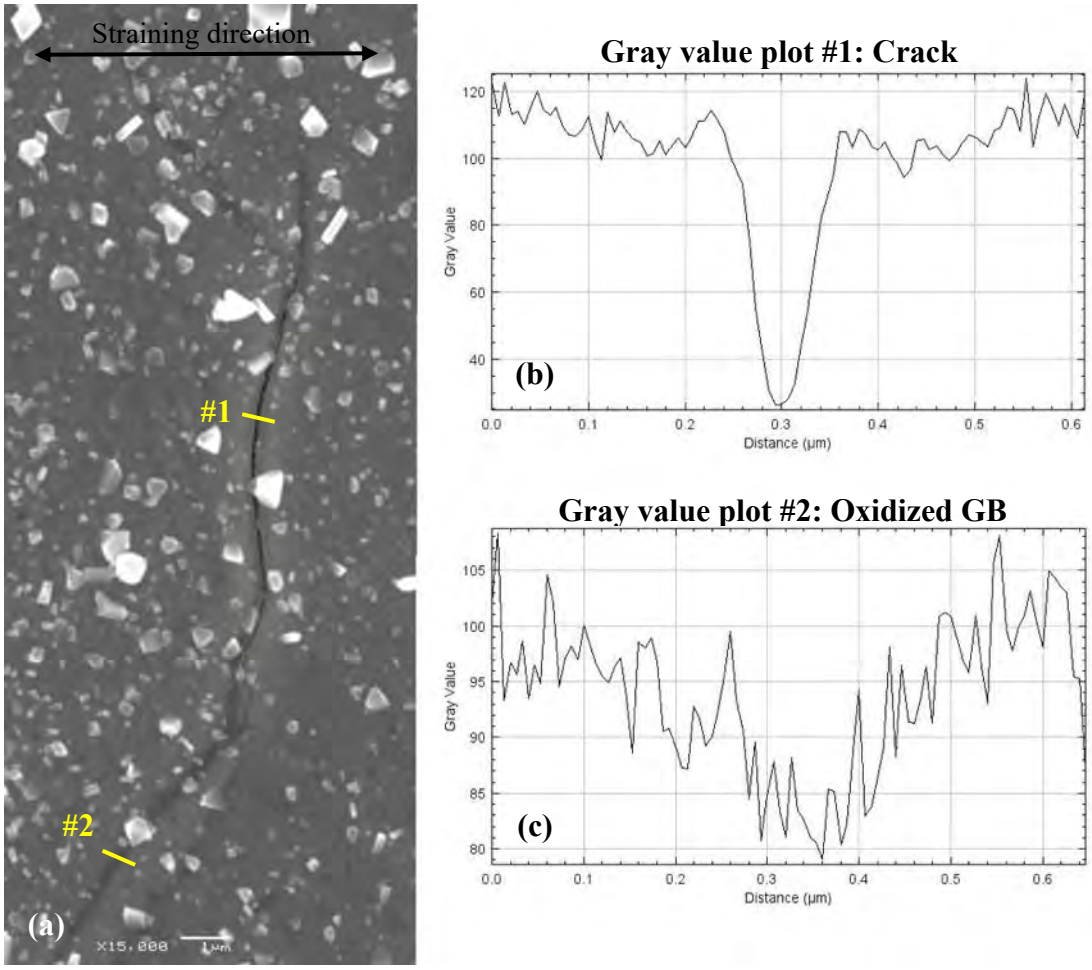

Figure 17. (a) The SE-image of the crack observed at the uniform strain region of B98-B1 (CW316 SS; 42 dpa) sample strained to 0.5YS, (b) gray value plot obtained from the crack and (c) gray value plot obtained from the oxidized grain boundary.

The SE image and the corresponding EDS elemental maps of another cracked location on the uniform strained region of B98-B1 (42 dpa) sample is shown in Figure 18. The elemental maps of O, Fe and Cr clearly shows that the larger crystallites at the grain interiors are Fe-rich whereas the formed Cr-Fe mixed oxides provide the template for it. Furthermore, depletion of Cr (see Figure 18d) can also be seen at these large crystallite oxides which are basically re-deposited from the testing condition. The Cr-map shows that the oxidized grain boundary is rich in Cr. The elemental maps of Fe and Cr clearly delineate the crack initiated at the oxidized grain boundary.

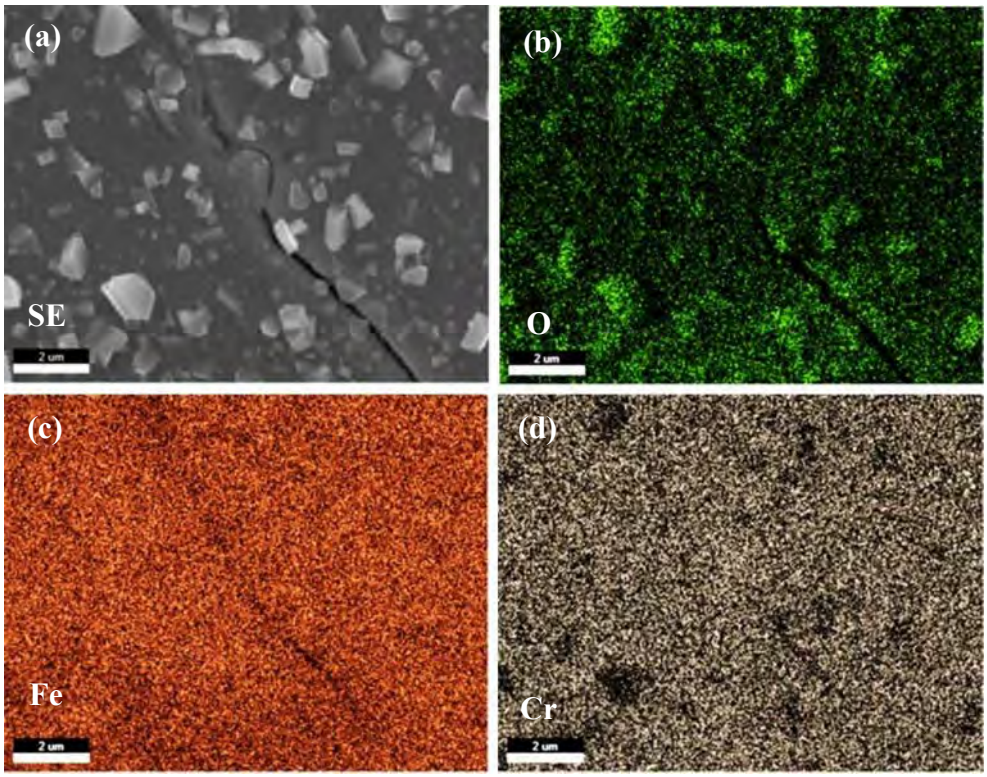

Figure 18. The EDS elemental mappings recorded from the cracked location of a sample B98-B1 (CW316 SS; 42 dpa) after straining to 0.5YS in PWR primary water environment, (a) SE image and (b-d) the corresponding EDS maps of O, Fe and Cr, respectively.

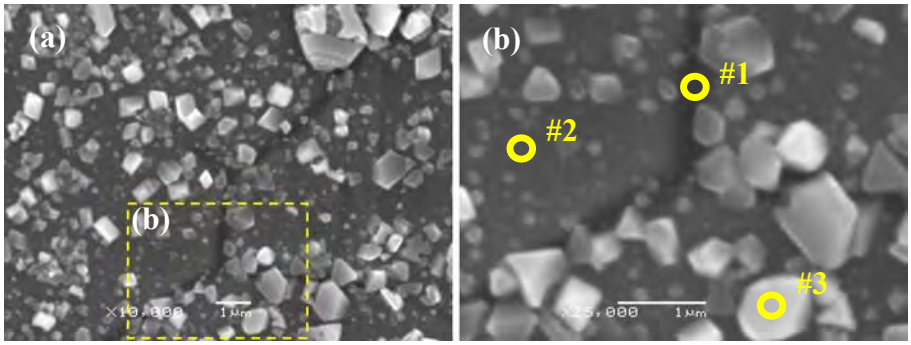

Figure 19. (a) The oxidized-only (uncracked) grain boundary triple junction in B98-B1 (CW316 SS; 42 dpa) strained to 0.5YS in PWR primary water, and (b) the enlarged SE micrograph of the yellow dashed portion marked in figure (a). Yellow circled area in (b) represents the EDS spot analysis location.

Table 9. The EDS-quantitative analysis obtained from the spot spectra at the oxidized-only (uncracked) GB region of a sample B98-B1 (42 dpa) strained to 0.5YS in PWR primary water.

Element	EDS spot #1		EDS spot #2		EDS spot #3	
	Wt.%	At.%	Wt.%	At.%	Wt.%	At.%
O	8.60	24.50	5.69	17.29	17.39	42.22
Cr	22.66	19.86	17.99	16.81	12.80	9.56
Fe	57.37	46.81	64.08	55.77	60.32	41.94
Ni	11.38	8.83	12.24	10.13	9.50	6.28

Figure 19 presents an oxidized (i.e. uncracked) grain boundary of a sample B98-B1 strained to 0.5YS in PWR primary water. The enlarged SE micrograph showing the oxidized triple junction and the EDS spot analysis (yellow circles in Figure 19b) were carried at our diffierent locations such as oxidized grain boundary, grain interior and the large crystallites at the surface. The quantification data of the spot #1 clearly shows that the oxidized grain boundary is rich in Cr, this means the grain boundaries are enriched with Cr-oxides. The concentration of Cr is higher than that in the grain interior. The EDS spot #3 clearly confirms that larger irregular shaped micron sized crystallites are Fe-rich oxides. The quantitative analysis of all the three spots were presented in Table 9.

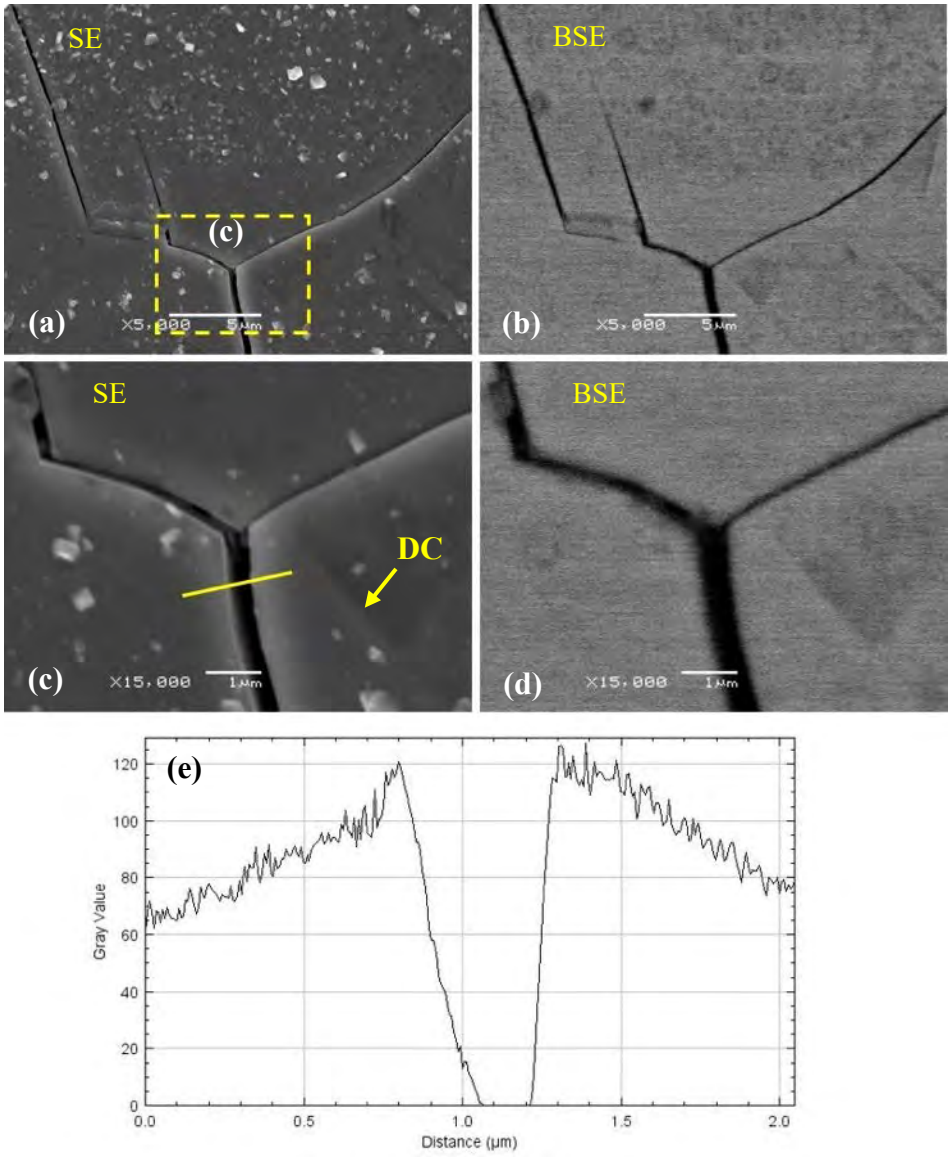

Figure 20. (a, b) SE and BSE images of a cracked triple junction observed in B98-B1 (CW316 SS; 42 dpa) sample after straining to 0.5YS in PWR primary water, (c, d) enlarged SE and BSE images of a dashed-yellow square in Fig. 20a, and (e) obtained gray value plot across (yellow line drawn in Fig. 20c) the cracked GB.

In the B98-B1 sample strained to 0.5YS, the cracks occurred at the non-oxidized grain boundary junction also. Figure 20 represents a location of the non-oxidized grain boundary triple junction captured in SE and BSE mode. The magnified SE and BSE micrographs shown in Figure 20c and 20d, clearly show a dislocation channel intersecting the GB near the crack site. As can be clearly seen in Figure 20c, the crack at the triple juncion is wider and the measured crack width based on the gray value plot is 497 nm (see Figure 20d). It should be noted that most of the cracks in this sample were observed at oxidized GB sites. However, in total, seventeen cracks were found in this sample out of which five of them were at non-oxidized GB with localized deformation as shown in Figure 20. Overall, the results show that intergranular

cracks nucleated in irradiated CW 316 SS sample B98-B1 (42 dpa) at a stress level (0.5YS) that is well below the yield stress. These results show that grain boundary oxidation, triple junctions, and dislocation channels are exhibited at the locations where crack initiation occurred.

Table 10. Cracking characteristics of the CW316 SS samples (dose levels: from 42 to 125. 4 dpa) upon single and interrupted straining four-point bend tests in PWR primary water environment.

Sample ID (CW316 SS)	Dose (dpa)	Stress (YS)	No. of cracks	Average crack length (μm)	Crack density (No. of cracks/mm^2)	Crack length/unit area (μm/mm^2)
B98-B1	42	0.5	17	70.9	9.7	688.9
B101-B1	46.9	0.4	0	0	0	0
		0.6	72	75	41.5	3130
		0.8	99	106.1	56.6	6005.2
B89-B1	67.4	0.4	0	0	0	0
		0.5	7	28.7	4	115.1
		0.6	43	35.5	24.6	860.3
B35-B1	125.4	0.4	0	0	0	0
		0.45	1	53.3	0.6	30.4
		0.5	15	28.2	8.6	241.5
		0.6	59	33.6	33.7	1134

To understand the cracking characteristics, the parameters such as average crack length, crack density (no. of cracks/mm^2), and crack length per unit area (i.e. total crack length divided by the analyzed area) are of special importance. In total, 17 cracks were observed on the B98-B1 (CW316 SS; 42 dpa) sample upon straining to 0.5YS in PWR primary water. Table 10 summarizes the cracking behavior of all the CW 316 SS with dose levels ranging from 42 to 125.4 dpa, investigated in this LWRS program. All of these irradiated CW316 SS bend samples were tested in a PWR primary water, at a constant strain rate with single or interrupted straining with small increments of stress.

3.3. Constant Load Four-Point Bend Test

The results of the four-point bend test at a constant load mode for two SA304 SS samples A84-1-2 (5.4 dpa) and A96-1-1 (95 dpa) are presented in this section. The bend load, LVDT displacement profile data and detailed SEM examination of the uniform strained region upon completion of the bend tests were presented. Small increment in stress, i.e. an interrupted straining at constant load mode was carried out

when no cracking observed at the first desired loading condition. Also, the cracks that initiated in the uniform strained region upon bend testing at constant load mode were characterized and quantified. A summary of the crack initiation stress and quantitative analysis of the cracks are tabulated.

3.3.1. Constant Load Test of SA304 SS (5.4 dpa and 95 dpa)

Bend sample A84-1-2 (SA304 SS; 5.4 dpa) was tested in constant load, four-point bend mode. The sample was strained to 0.5YS at a strain rate of 4.3×10^{-7}/s in a simulated PWR primary water environment, and then held at that stress for 200 h at this applied load condition. Upon completion of the 200 h test, the crosshead was immediately reversed and returned to the initial set point, after which, the uniform strain region of the sample was analyzed in SEM. Figure 21 presents the LVDT displacement and load data during the four-point bend test in constant load mode for 200 h in PWR primary water. It has been reported earlier [1] that a bend sample A84-1-1 with the same dose (5.4 dpa) was strained in a constant strain rate mode in an interrupted manner with stress increments of 0.5, 0.6 and 0.7YS. Cracks were found only after straining to 0.6YS in the constant strain rate (interrupted) test whereas in the constant load mode, the sample A84-1-2 (5.4 dpa) cracked at 0.5YS.

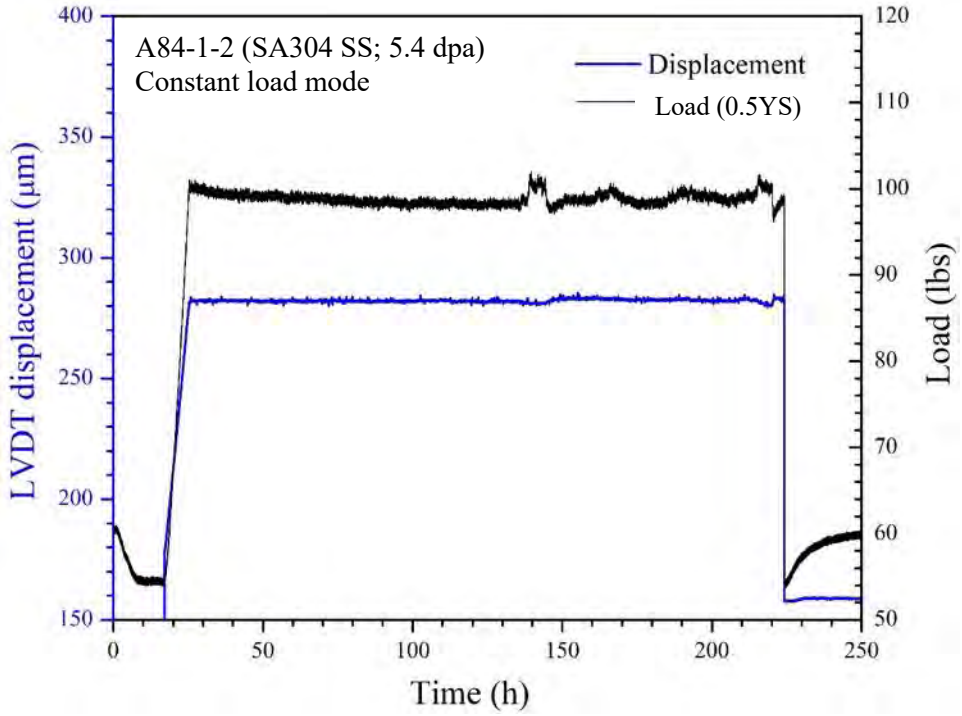

Figure 21. Load and LVDT displacement data of a sample A84-1-2 (SA304 SS, 5.4 dpa) upon straining to 0.5YS for 200 h in PWR primary water.

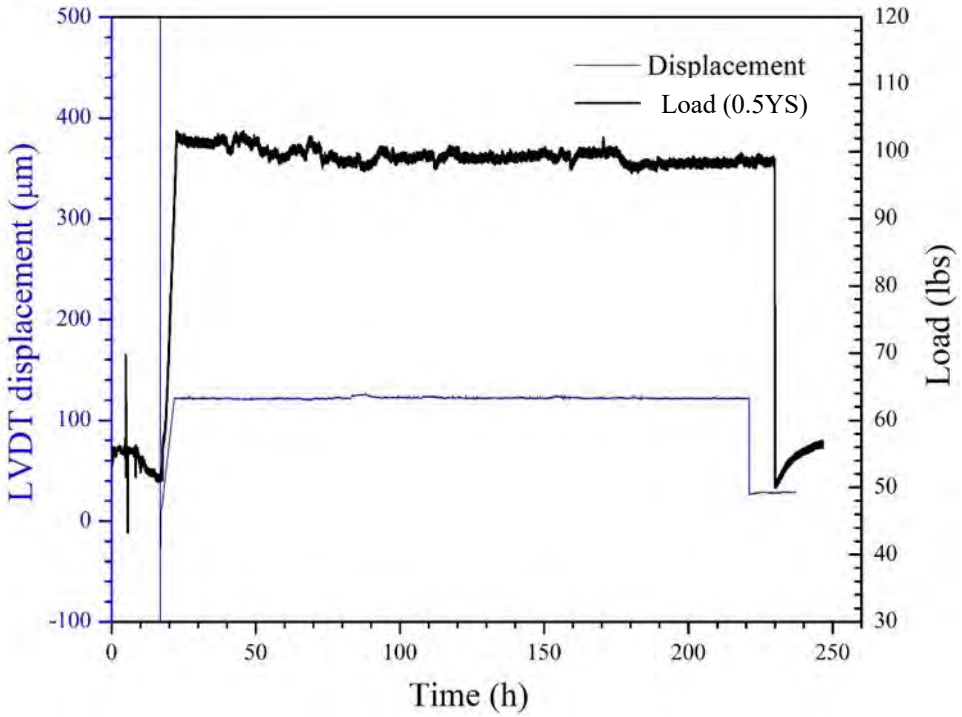

Figure 22. Load and LVDT displacement data of a sample A96-1-1 (SA304 SS, 95 dpa) upon straining to 0.5YS for 200 h in PWR primary water.

As described before at the beginning of this section, bend sample A96-1-1 (SA304 SS; 95 dpa) was also tested in the constant load four-point bend test method. It should be noted that the sample A96-1-2 of the same dose level (95 dpa) initiated cracks upon straining in constant strain rate mode to 0.6YS of the irradiated yield strength in simulated PWR primary water. Therefore, the constant load mode bend test for the sample A96-1-1 (95 dpa) was conducted at 0.4YS for 200 h. The sample was then examined in SEM, and no cracking occurred. As a next step, the sample was tested again in constant load mode at a value of 0.5YS for 200 h in simulated PWR primary water. Figure 22 shows the LVDT displacement and load data during constant load bend test carried out for the sample A96-1-1 (95 dpa) at 0.5YS for 200 h in high temperature water. The uniform strain region of this sample was then characterized in SEM and cracks were found upon straining to 0.5YS in constant load bend test for 200 h. Table 11 summarizes the results of the constant strain rate and constant load tests on A84 and A96 samples.

Table 11. The crack initiation stress for the SA304 SS samples with various dose levels.

Sample ID	Dose (dpa)	Four-point bend test condition	Initiation stress (YS)
A84-1-1	5.4	Interrupted straining at constant strain rate: 0.5, 0.6, and 0.7 YS	0.6
A84-1-2	5.4	Constant load for 200 h: 0.5YS	0.5
A96-1-2	95	Interruptedly strained twice at constant strain rate: 0.6YS	0.6
A96-1-1	95	Interrupted straining at constant load for 200 h in each stress level: 0.4 and 0.5YS	0.5

3.3.2. Characterization of Grain Boundary Oxidation and Cracking

Bend sample A84-1-2 (SA304 SS; 5.4 dpa) exposed to simulated PWR primary water for 200 h at a stress of 0.5YS was examined using SEM and examples of oxidation and cracking are presented in this sub-section. Heavily oxidized grain boundaries and the emergence of dislocation channels were noted in the uniform strain region of this constant load mode bend tested sample, as presented in Figure 23. This is one example of an oxidized grain boundary triple junction.

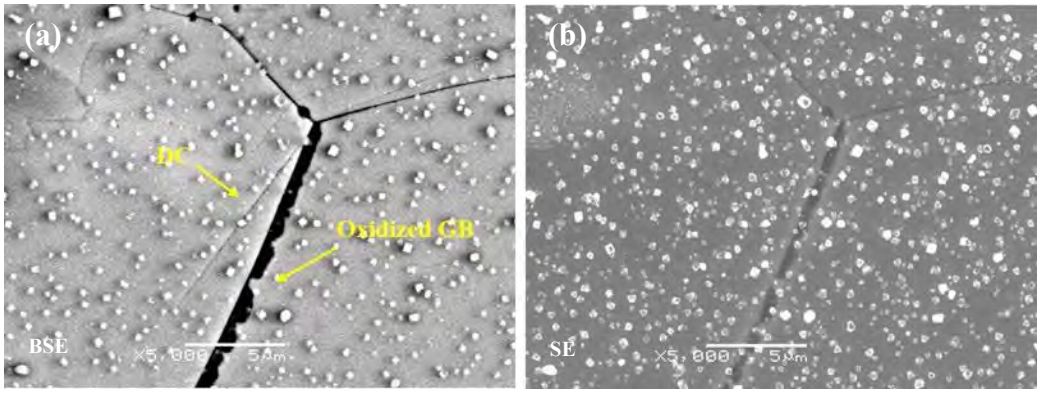

Figure 23. BSE (a) and the corresponding SE (b) images showing the oxidized grain boundary and the dislocation channel (DC) in the uniform strained region of a sample A84-1-2 (SA304 SS; 5.4 dpa) after completion of 0.5YS-constant load four-point bend test in PWR primary water for 200 h.

Figure 24 is another representative location of the same sample (A84-1-2) illustrating the co-existence of the oxidized triple junction and the dislocation channel in the uniform strain region. As shown in Figure 23a and 24a, the dislocation channels can be seen more clearly in BSE images in which the dark contrasted grain boundary represents the oxidized state. The DC-GB intersection site (yellow-dashed box in Figure 24a) was enlarged, and captured in SE-mode (see figure 24b). The microchemistry of the oxidized grain boundary was determined via an EDX line scan across the boundary as shown in Figure 24b. From line scan #1 (Figure 24c) it is clear that the attacked grain boundary is depleted with Fe. The line scan #2 (Figure 24d) was measured across the oxidized GB where the DC intersects the boundary, and it shows that the grain boundary oxide is enriched in Cr. The crystallites distributed throughout the surface are Fe-rich oxides.

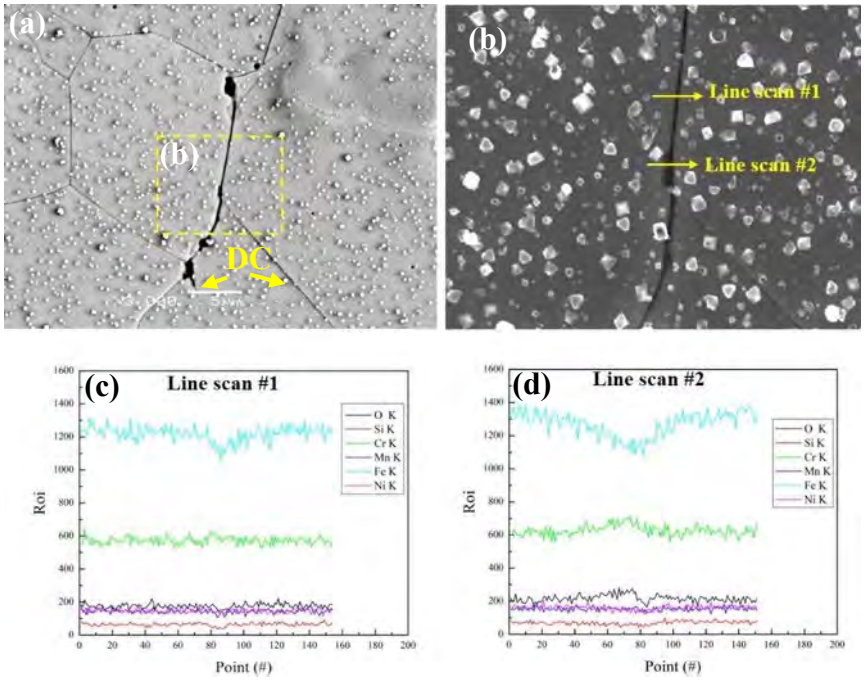

Figure 24. (a) Plan view BSE-image illustrates the development of DC and the oxidized grain boundary triple junction in constant load bend tested sample A84-1-2 (5.4 dpa), (b) SE-image of the enlarged portion of the yellow-dashed box in figure 24a, and (c-d) the line scan profiles measured across the oxidized grain boundary at locations with and without DC intersection.

Exposing the sample to in a constant load test at 0.5YS for 200 h in PWR primary water leads to several cracks. The BSE image presented in Figure 25a identifies a crack at the severely oxidized grain boundary. The magnified BSE-image (see, Figure 25b) clearly shows the DC-GB intersection site where the crack initiated at the severely oxidized GB. Further zooming in and capturing the image in SE mode (Figure 25c), clarifies the crack as well as the oxidation in that boundary. An EDX line scan measurement across the cracked grain boundary is presented in Figure 25d and demonstrates that the cracked grain boundary is heavily oxidized, and this grain boundary oxide is enriched with Cr.

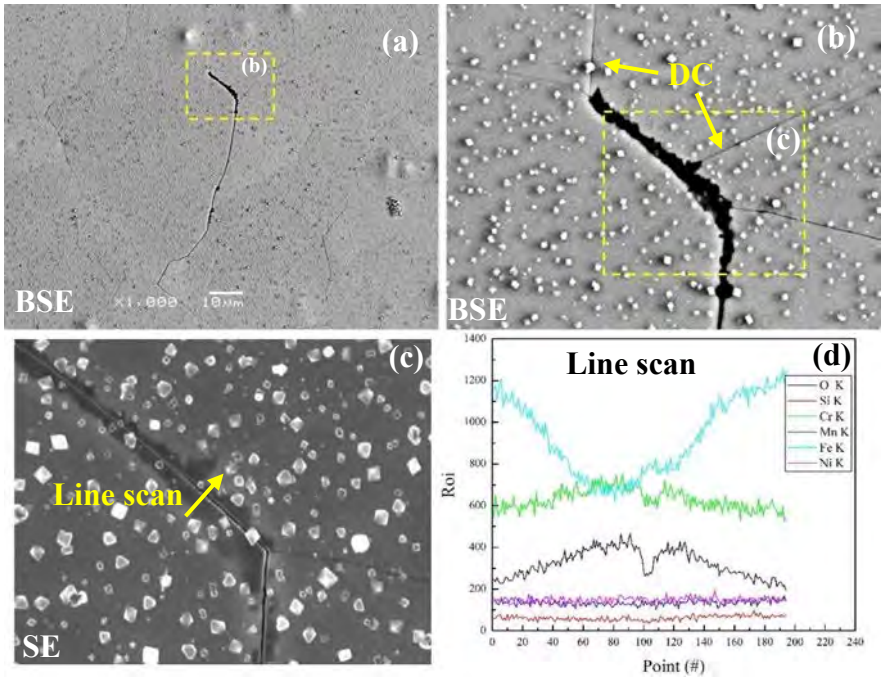

Figure 25. (a-c) Surface morphology of the DC-GB intersection site observed on a sample A84-1-2 (5.4 dpa) after completion of 0.5YS-constant load four-point bend test in PWR condition, and (d) the line scan across the fractured boundary that was oxidized severely.

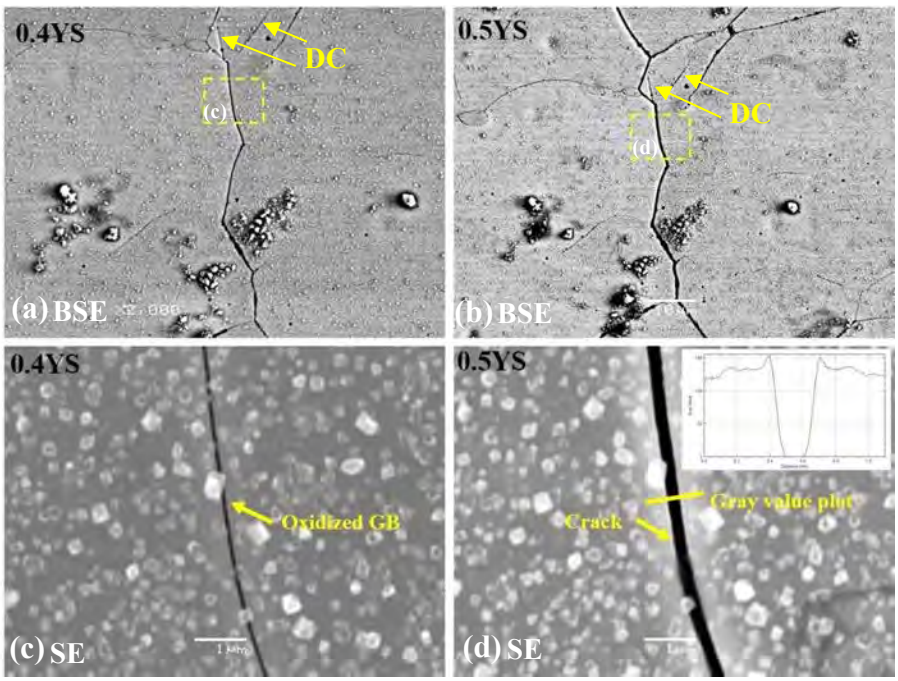

Figure 26. (a) and (c) Oxidized state of the GB in A96-1-1 (95 dpa) sample exposed to 0.4YS-constant load test for 200 h, and this oxidized GB was cracked upon exposing to 0.5YS-constant load test for 200 h, (b) and (d) shows the cracked GB. Inset: Gray value plot measured across the cracked GB, shown in (d).

It has been reported [1] that bend sample A96-1-2 initiated multiple cracks when subjected to 0.6YS at a constant strain rate four-point bend test. Further straining in the same loading condition (i.e. strained twice

to 0.6YS) generated many new cracks, also some small cracks coalesced and grew into a long and/or wide crack [1]. Another sample with the same dose, A96-1-1 (95 dpa), was strained to 0.4YS and held for 200 h (i.e. constant load mode) in PWR primary water environment. No cracks initiated at this test condition, but the generation of DC and oxidation of grain boundaries were observed. As there was no cracking occurred after straining to 0.4YS, another constant load test was conducted at 0.5YS.

Representative SEM-micrographs (Figure 26) illustrates the oxidation of GB in a constant load test at a stress of 0.4YS and cracking in the subsequent constant load test at a stress of 0.5YS. The BSE image Figure 26(a) and the enlarged SE-image Figure 26(c) (dashed-yellow box of Figure 26a) represent the oxidized state of GB in bend sample A96-1-1 (95 dpa) exposed to 0.4YS-constant load test for 200h. DCs were generated at this stress level; two DCs intersecting the GB can be seen in the BSE image at 0.4YS. As a result of oxidation, the GB appears to be darker and wider than the neighboring GB. This oxidized GB cracked after loading to 0.5YS in the subsequent constant load test. The enlarged SE image in Figure 26(d) shows the cracked GB and the inset shows the gray value plot measured across the cracked GB. The two DCs intersecting the oxidized GB caused stress concentration and likely led to crack initiation.

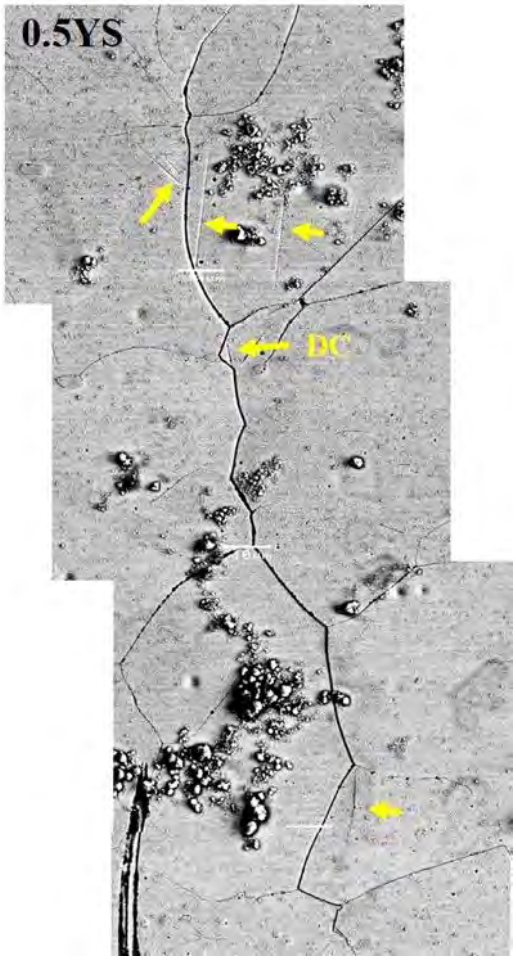

Figure 27. The stitched BSE image shows an example of long crack grown with more DCs in bend sample A96-1-1 (95 dpa) upon completion of 0.5YS-constant load test.

As shown in the Figure 27, more DCs were observed with the higher stress level of 0.5YS along with the initiation of cracks. Apart from more DCs, this cracked location has many triple junctions. It should be noted that the reported crack initiation stress for this dose level (95 dpa) was 0.5YS in the constant load experiment. At 0.4YS constant load exposure oxidation of grain boundary occurred and further incremental in stress level to 0.5YS constant load exposure initiated the cracks, but their average length is comparable to that of cracks initiated at 0.6YS- strained twice in an interrupted manner. Table 12 summarizes the crack characteristics that were formed in sample conditions A84 and A96 (with dose levels 5.4 and 95 dpa) tested in various of modes of four-point bend tests.

Table 12. Cracking characteristics of the sample conditions A84 and A96 (dose levels: 5.4 and 95 dpa) tested in series of constant strain rate and constant load mode four-point bending tests.

Sample ID	Dose (dpa)	Four-point bend test method	Stress (YS)	No. of cracks	Avg. crack length (μm)	Crack density (No. of cracks/mm^2)	Crack length/unit area (μm/mm^2)
A84-1-1	5.4	Interrupted straining in PWR primary water	0.5	0	0	0	0
			0.6	5	58.1	2.9	166
			0.7	17	62.8	9.7	610.2
A84-1-2	5.4	Constant load for 200 h in PWR primary water	0.5	4	136.9	2.3	312
A96-1-2	95	Interrupted straining in PWR primary water, with the same loading condition	0.6	16	76.4	9.1	698.5
			0.6	26	157	14.8	2333
A96-1-1	95	Constant load for 200 h in each step	0.4	0	0	0	0
			0.5	6	130.7	3.4	448.1

3.4. Separation of Oxidation and Straining

Two samples of SA304 SS with dose level of 69 dpa (A98-1-1 and A98-3) were pre-oxidized followed by straining in an inert environment. The sample A98-1-1 underwent an oxidation without application of load in 320°C PWR primary water for 210 hr. The oxidized sample was then strained in high temperature Ar. In this way the oxidation process was separated from the straining step. The results obtained from the pre-oxidation step, cracking behavior of the pre-oxidized sample when strained in argon gas, and a sample simply strained alone in argon are presented in this section. It was reported that the crack initiation stress determined through the interrupted straining experiments in high temperature water of the same dose level sample A98-1-2 (69 dpa) was 0.8YS [1]. Therefore, to understand the role of straining in PWR primary

water on IG cracking, these new sets of experiments were conducted with the objective of separating oxidation and straining.

3.4.1. Pre-Oxidation of SA304 SS (69 dpa) in PWR Condition

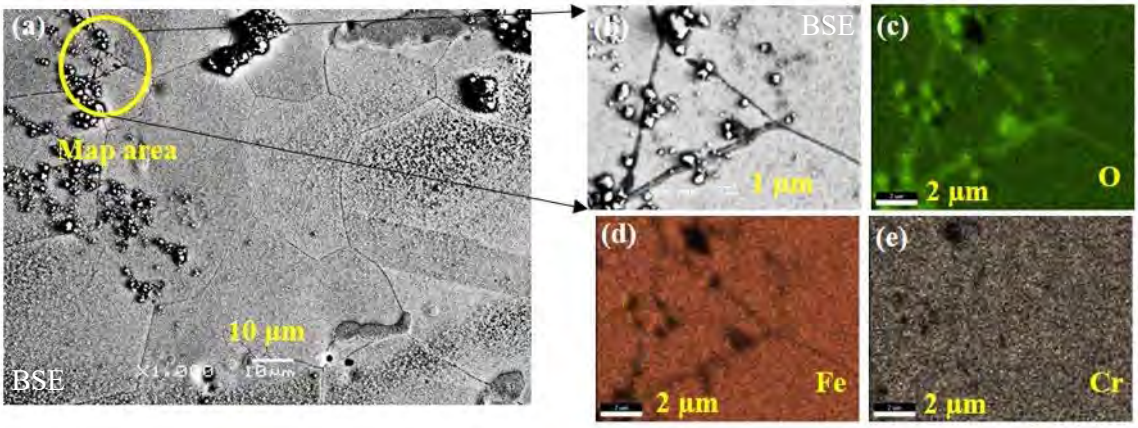

Figure 28. The SEM-EDX analysis of a bend sample A98-1-1 (SA304 SS; 69 dpa) after 210 h of oxidation at 320 ℃ in simulated PWR primary water, (a) plan view BSE image, and (b-e) enlarged BSE image and the corresponding EDS-maps.

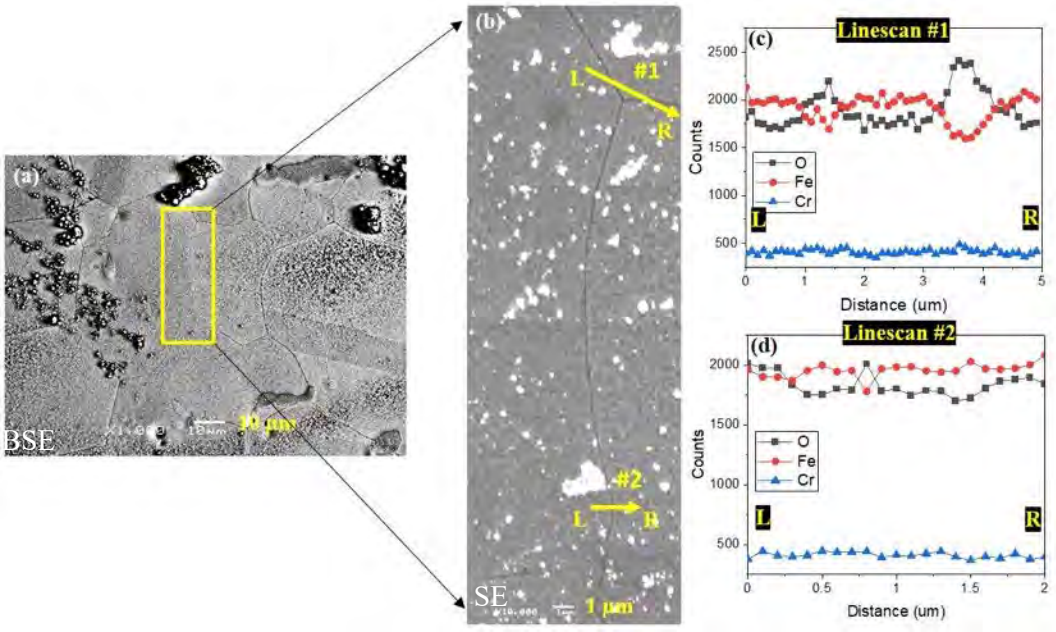

Figure 29. The SEM-EDS analysis of a bend sample A98-1-1 (SA304 SS; 69 dpa) after 210 h of oxidation at 320 ℃ in simulated PWR primary water, (a) plan view BSE image, (b-d) enlarged (stitched) SE image and the line profiles across the oxidized GBs**.**

The bend sample A98-1-1 (SA304 SS; 69 dpa) was exposed without application of load to the PWR primary water environment at 320 ℃ for 210 h. Then, the oxidized surface was imaged using SEM-EDS

to reveal that several GBs were heavily oxidized. The darker and wider GBs appear in a BSE-image the greater the amount of oxidation. An example of heavily oxidized/attacked GBs with the corresponding EDS map is shown in Figure 28. The oxygen map clearly shows that the dark regions are rich in O indicating oxidation of the GB region. The Fe map and Cr map indicate that Fe is depleted and Cr is enriched in the GB oxides.

The stitched SE-image presented in Figure 29b shows the severity of oxidation, i.e. to distinguish the attacked (or heavily oxidized) and the non-attacked GBs. The oxygen line profile in the EDS line scan #1 across the GBs shows that the O signal for the GB at the right side is wider than the one at left side. This indicates that the GB at the right side is more heavily oxidized than the one at the left side of the triple junction (see Figure 29b). By comparing the O signal tendency of the line scan #2 and line scan #1, it clear that the horizontal GB is more heavily oxidized than the vertical GB. Moreover, the GBs are depleted in Fe, indicating that GBs are Cr-rich oxides. As known already, the outer (micron/sub-micron size) distributed crystallites are Fe oxides due to redeposition.

3.4.2. Ar Straining of Pre-Oxidized SA304 SS (69 dpa)

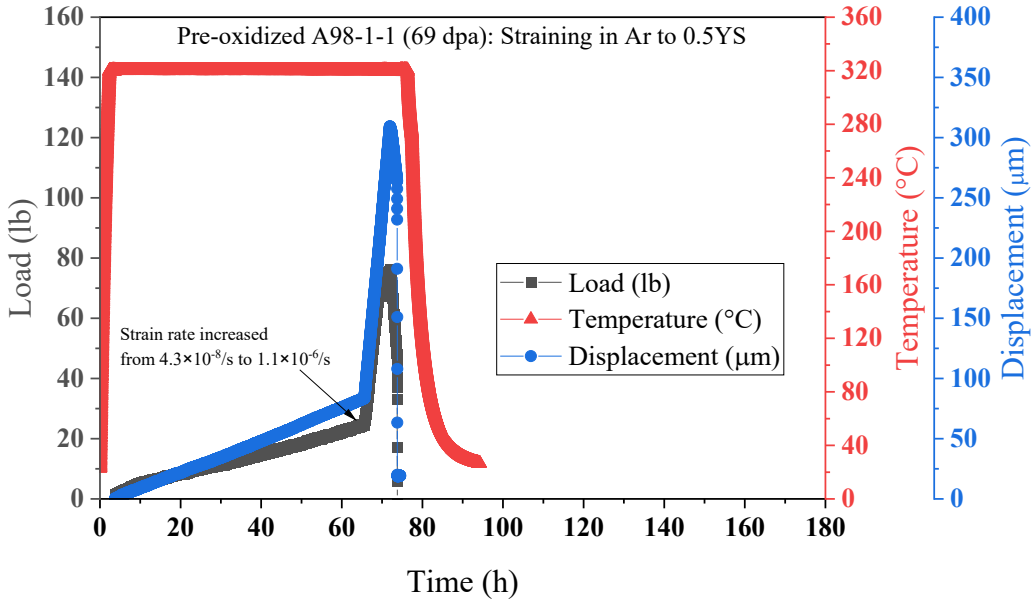

Figure 30. The thermal profile, load and LVDT displacement data during straining of a pre-oxidized sample A98-1-1 (SA304 SS; 69 dpa) in Ar (0.215 l/min).

The pre-oxidized bend sample A98-1-1 (SA304 SS; 69 dpa) was then strained to 0.5YS in an inert argon gas atmosphere with a flow rate of 215 ml/min. The temperature profile, load and LVDT displacement data are presented in Figure 30. At the beginning, straining was carried out with a standard strain rate 4.3×10^{-8}/s until 14% of the yield stress, then switched to 1.1×10^{-6}/s (i.e. 25x higher than the standard one). Due to an inert argon gas flowing atmosphere, there was no oxidation/corrosion. After reaching the desired load, the crosshead was returned to its set point. Upon completion of the Ar straining, the uniform strained region of the sample was then examined in SEM.

3.4.3. Crack Characteristics

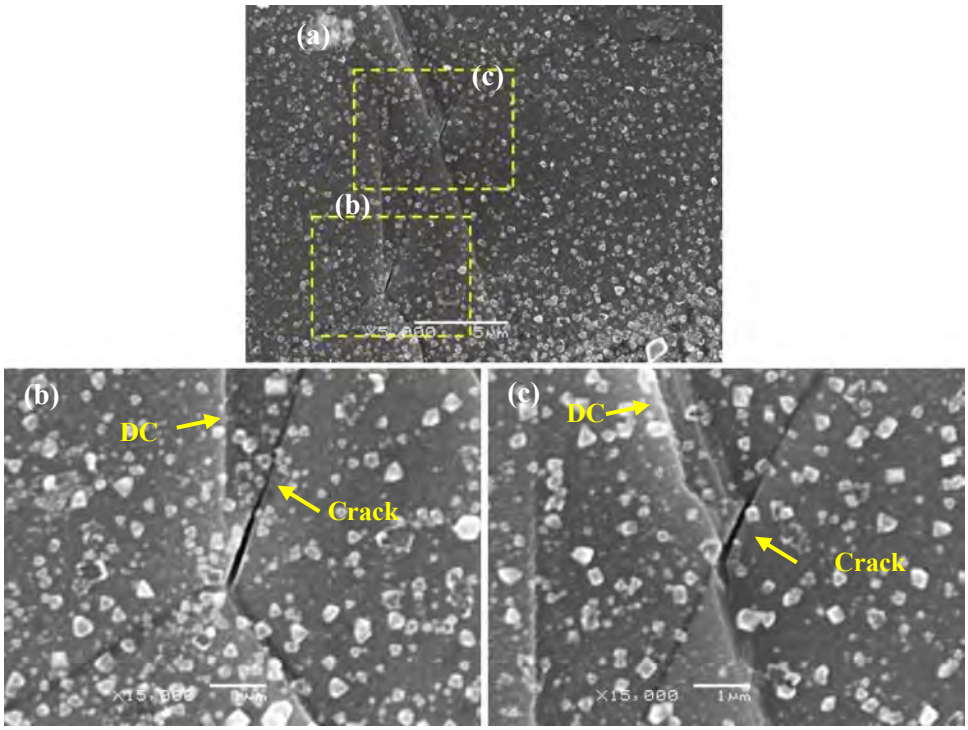

Figure 31. SE-images of the cracks observed after Ar straining of a pre-oxidized A98-1-1 (SA304 SS; 69 dpa) sample, the enlarged SE-images (b) and (c) show a crack at the DC-GB intersection.

Table 13. Bend test results of the pre-oxidized A98-1-1 (69 dpa) after straining in Ar to 0.5YS.

Sample ID	Stress (YS)	No. of cracks	Average crack length (μm)	Crack No. density (#/mm^2)	Length density (μm/mm^2)
A98-1-1	0.5	11	2.2	6.3	13.9

The pre-oxidized bend sample A98-1-1 (SA304 SS; 69 dpa) exhibited several cracks after straining to 0.5YS in high temperature argon gas environment. Straining in an inert condition is to avoid any environmental contributions on IG cracking of the pre-oxidized sample. As described earlier, the pre-oxidation in PWR primary water at 320 °C for 210 h led to oxidation of the grain boundaries, in particular, Cr-rich oxides, and the randomly distributed crystallites at the surface are rich in Fe-oxides from the re-deposition. Upon straining the pre-oxidized sample to 0.5YS in Ar, cracks were initiated at the intersections between dislocation channels and oxidized grain boundary. Figure 31 presents the representative SE-micrographs showing the cracks where the dislocation channels intersects the oxidized grain boundary. It can be seen very clearly in the enlarged SE images shown in Figures 31b and 31c. In particular, Figure 31b illustrates initiation of a crack at a location where a DC intersects the oxidized GB triple junction. Overall, eleven cracks were observed, and quantification of cracking characteristics is provided in Table 13. It should be noted that all the observed cracks were associated with or occurred at the DC-GB intersections.

3.4.4. Ar straining of as-irradiated SA304 SS (69 dpa)

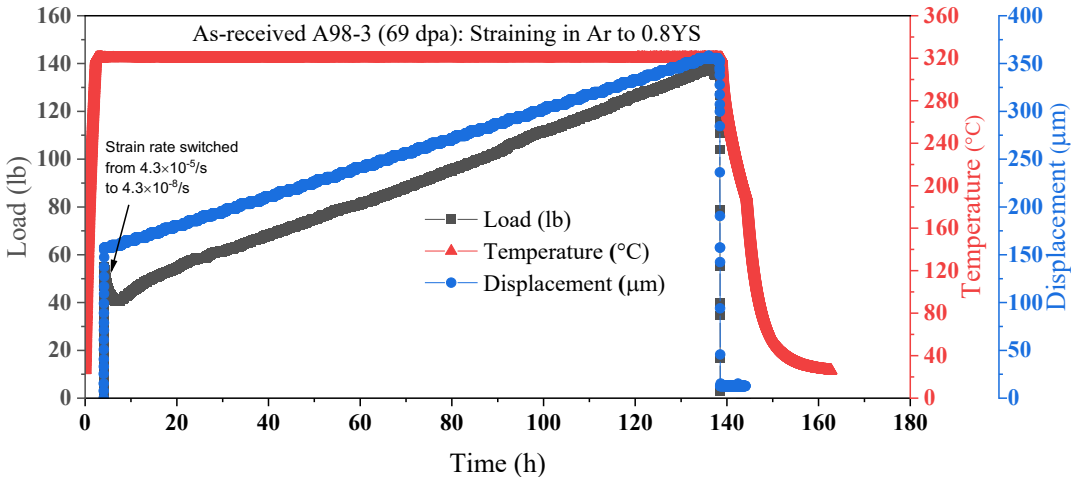

Figure 32. Thermal profile, load and displacement data during straining of an as-received irradiated sample A98-3 (SA304 SS; 69 dpa) in Ar (0.215 l/min).

It should be noted that the bend sample of same dose level (69 dpa) tested at a constant strain rate in simulated PWR primary water revealed IG cracking at 0.5YS, and the crack initiation stress was obtained through an interrupted straining with small increments in stress level (i.e. 0.5, 0.6, 0.7 and 0.8YS) [1]. On the other hand, the sample that was pre-oxidized in PWR condition for 210 h and subsequently strained in high temperature Ar initiated the cracks at 0.5YS. So, the purpose of straining an as-received neutron irradiated sample (69 dpa) in high temperature argon is to rule out intrinsic susceptibility to IG cracking and to demonstrate that IG crack initiation occurs by rupture of oxidized grain boundaries. As-received neutron irradiated bend sample A98-3 (SA304 SS; 69 dpa) was strained to 0.8 of the irradiated yield strength in an inert argon gas atmosphere. The straining was carried out at 320 ℃ in argon gas with a flow rate of 215 ml/min. To mimic the tare load condition that sample experience in PWR primary water environment, increased strain rate of 4.3×10^{-5}/s was used at first, and switched then to a standard strain rate of 4.3×10^{-8}/s until the desired load, i.e. 0.8YS. Figure 32 presents the thermal profile, load and displacement curve during straining of an as-received neutron irradiated A98-3 (69 dpa) in an inert argon gas environment. Upon completion of the straining in argon, the uniform strained region of a sample was then fully characterized using SEM and the representative images are presented in Figures 33 and 34.

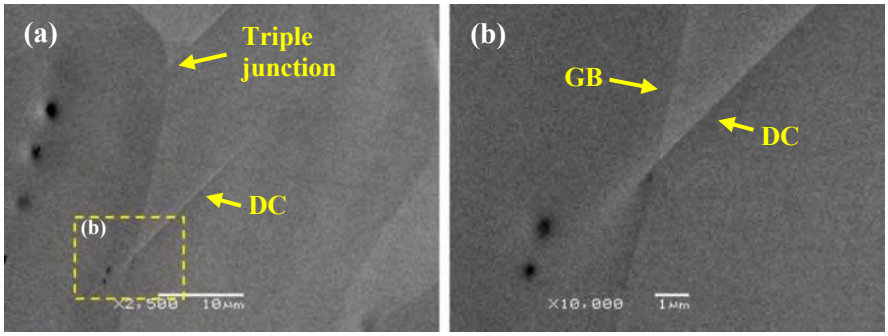

Figure 33. SE-images captured upon straining of an as-received A98-3 (SA304 SS; 69 dpa) sample to 0.8YS in high temperature Ar, (a) oxide free GB junction with DC and (b) no cracking observed at the DC-GB intersection.

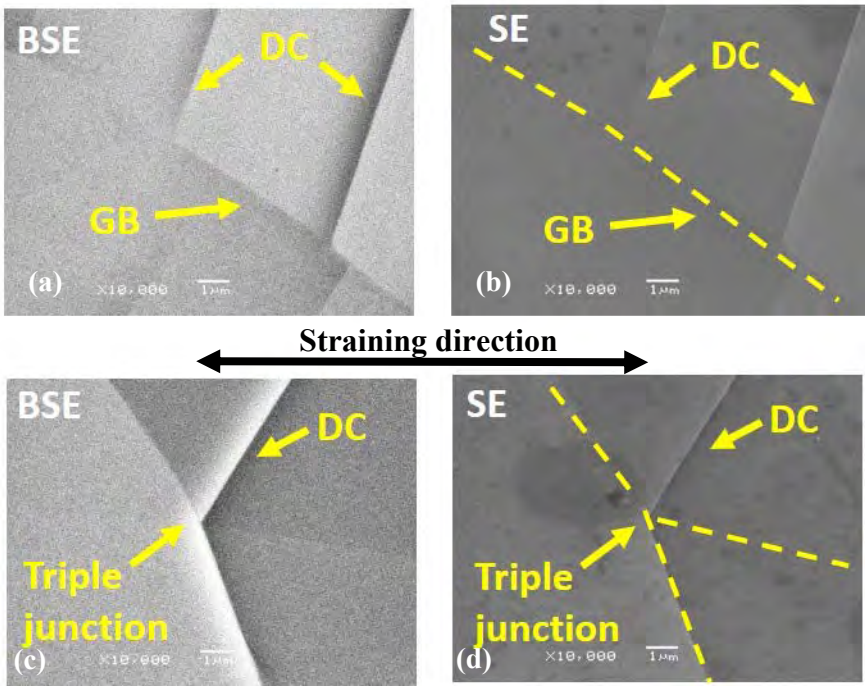

Figure 34. BSE and SE-images captured upon straining of an as-received A98-3 (SA304 SS; 69 dpa) sample to 0.8YS in high temperature Ar, showing the DC-GB intersection sites with no evidence of cracking.

As shown in the SE and BSE micrographs shown in Figures 33 and 34, the surface was notably oxide free due to straining in an inert argon gas environment and the dislocation channel intersections with grain boundaries were clearly observed. However, no intergranular cracking occurred upon straining in Ar. On the other hand, the pre-oxidized sample showed cracking upon straining in argon at 0.5YS, and the sample strained in PWR primary water showed cracking at 0.8YS. The quantitative analysis of cracking occurred in 69 dpa samples in various four-point bend test conditions were summarized in Table 14.

Table 14. Cracking characteristics of SA304 SS (69 dpa) in various test conditions.

Sample ID	Dose (dpa)	Four-point bend test method	Stress (YS)	Number of cracks	Average crack length (μm)	Crack density (No. of cracks/mm^2)	Crack length/unit area (μm/mm^2)
A98-1-2	69	Interrupted straining in PWR primary water	0.5	0	0	0	0
			0.6	0	0	0	0
			0.7	0	0	0	0
			0.8	7	39.2	4	156
A98-1-1	69	Sample pre-oxidized in PWRcondition for 210 h, strained in Ar	0.5	11	2.2	6.3	13.9
A98-3	69	Straining in Ar	0.8	0	0	0	0

3.5. Microstructures and Microchemistries of HAGBs in strained B35-B1 (CW316 SS; 125.4 dpa) and A84-1-1 (SA304 SS; 5.9 dpa) samples

3.5.1. HAGBs in strained B35-B1 (CW316 SS; 125.4 dpa) sample

Figure 35a is a HAADF image taken from an attacked HAGB in B35-B1 (strained CW316 SS; 125.4 dpa) in which no cracks were seen. Instead, a large, irregular region showing darker contrast surrounding to the GB was formed (Fe-rich oxide). Nanobeam electron diffraction (NBED) patterns were taken from the two oxide (outlined by green circles) and two matrix (outlined by red circles) shown as insets in Figure 35a, which are two superimposed NBED patterns from the oxide (green color spots) and the matrix (red color spots). The NBED patterns from the red regions were indexed as <110> of the FCC matrix. The NBED pattern from the green regions can be indexed as FCC phase, with a lattice parameter of 0.82nm along its <110> direction. Figures 35b-f are corresponding element maps from imaged area in Figure 35, which indicate that the darker region consists of mainly O, Cr, and Fe and some Ni. So it is very possible that this phase has the spinel $CrFe_2O_4$-type structure, i.e., $(Cr_x,Ni_{1-x})Fe_2O_4$ growing epitaxially from the matrix during oxidation. It should be indicated that the spinel-type oxides formed at each side of the original GB still share the same GB (as shown in Figure 35a) with the same GB angle. Outside this phase, there formed a thin Cr-rich oxide layer extended to the sample surface with a thin Ni-rich oxide layer formed underneath as indicated by white arrows in the maps. At the end of the attacked GB, enhanced Ni (~1.8 times more Ni over the RIS Ni-rich GB) segregation to the GB was seen which extends down to about 100nm depth along the GB. Also, Si is still rich along the GB except the top ~200nm segment.

Figure 36a is a HAADF image taken from B35-B1 (strained CW316 SS; 125.4 dpa) sample showing a long crack formed along a GB besides another attacked GBs in the upper left. Figures 36(b-f) are element maps from the region. Results indicate that the surfaces of the flanks of the crack consist mainly the $(Cr_x,Ni_{1-x})Fe_2O_4$ spinel phase. Then a thin Cr-rich oxide layer with a thin Ni-rich oxide layer underneath as indicated by white arrows in the maps. The GB at the crack tip has enhanced Ni segregation (~1.2 times more Ni over the RIS Ni-rich GB) extending to ~100nm along the GB. Si seems to have gone from the GB (The strong Si signal in the crack is an artifact during the map quantification due to weak Si signals). The attacked GB in the image in Figure 36a shows similar microchemistry to that of the GB in Figure 35.

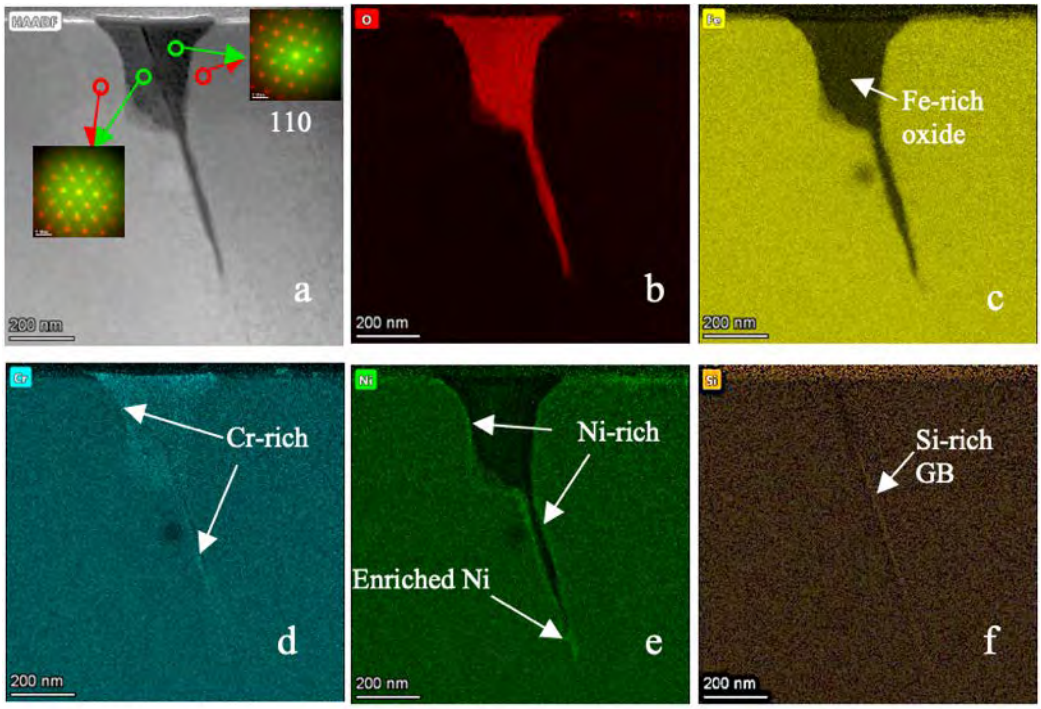

Figure 35. a) HAADF image showing a HAGB in B35-B1 (strained CW316-SS; 125.4 dpa) sample with NBED patterns collected from the 4 circled regions; b-f are O-map, Fe-map, Cr-map, Ni-map and Si maps collected from the imaged area in a, respectively.

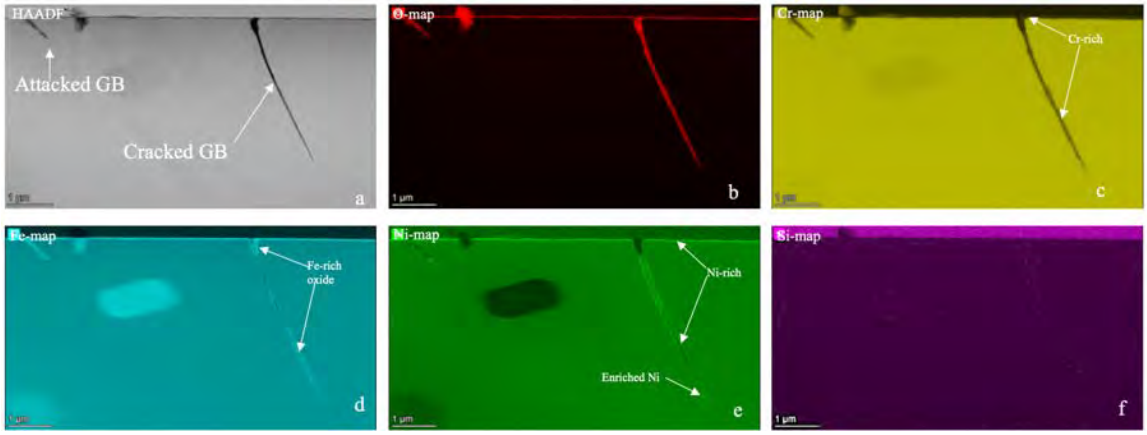

Figure 36. a) HAADF image showing a HAGB with a long crack in B35-B1 (strained CW316 SS; 125.4 dpa) sample and two attacked GBs; b-f are O-map, Cr-map, Fe-map, Ni-map and Si maps collected from the imaged area in a, respectively.

3.5.2. HAGBs in strained A84-1-1 (SA304 SS; 5.4 dpa) sample

Figure 37a shows a HAADF image taken from A84-1-1 (strained SA304 SS; 5.4 dpa) with an attacked GB indicated by a white arrow. A dark region covering the sample surface and down to about 50 nm deep into the GB was seen to form. Figures 37 b-f are element maps from the region showing the distribution of O, Cr, Ni, and Fe. It indicates that the attacked GB region consist of O, Cr, Fe, and some Ni. A key feature is that the GB has enriched Ni concentration (~3.0 times more Ni over the RIS Ni-rich GB) beyond the attacked end down to ~200 nm depth. Figures 37 (f-j) show element mapping data collected from another attacked GB in the same sample but with deeper attack down to around 200 nm. Besides forming Fe-rich oxide particles on the surface of the sample, Fe also coexists with Cr forming a mixed oxide phase on the surface of the sample as well as in the attacked GB region. Underneath, there is also a thin Ni-rich oxide layer formed as indicated by white arrows in the maps. More interestingly, at the end of the attacked GB, the enhanced Ni-rich GB (~3.0 times more Ni over the RIS Ni-rich GB) was seen to extend shorter ~ 100nm.

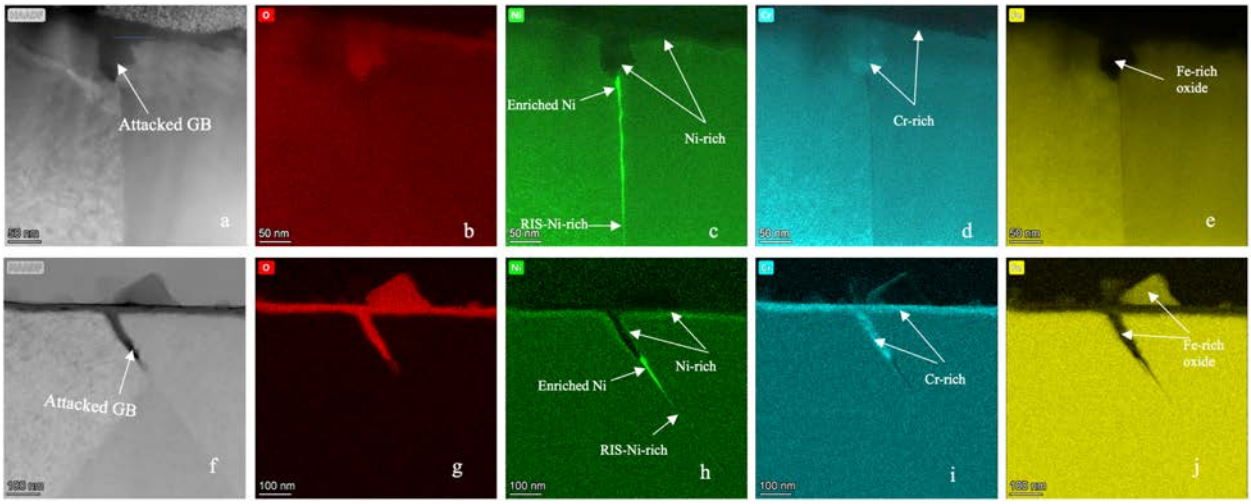

Figure 37. a) HAADF image showing an attacked HAGB in A84-1-1 (strained SA304 SS; 5.4 dpa) sample; b-e are O-map, Ni-map, Cr-map, and Fe-map collected from the imaged area shown in (a), respectively. Figure (f-j) show STEM-SI EDS mapping data from another attacked GB in the same sample but being attacked deeper.

The same GB shown in Figure 37f was also studied by STEM-SI EELS after it had been further thinned. As a much small electron beam was used (~0.1 nm), more detailed element distribution information can be obtained besides the enhanced O signals, thus better O map contrast. Results shown in Figure 38 further confirm that the surface of the sample is covered with a thin Cr-rich oxide layer along with some large Fe-rich oxide particles. Underneath, a Fe/Cr-rich oxide layer was formed which extended to the attacked GB region. In between the mixed oxide layer and the matrix, a thin Ni-rich layer was seen. Again, the enhanced Ni segregation was found at the end of the attacked GB and appears much brighter in the Ni-map.

Figure 39 shows microstructures of a cracked triple junction in A84-1-1 (strained SA304 SS; 5.4 dpa) sample. High resolution HAADF imaging reveals that the cracked GBs are filled with fractured spinel $CrFe_2O_4$-type oxide growing epitaxially from one nearby grain with either $<211>_{matrix}$// $<110>_{oxide}$ (GB-3) or $<110>_{matrix}$// $<110>_{oxide}$ (GB-2 and GB-1 confirmed by SAED).

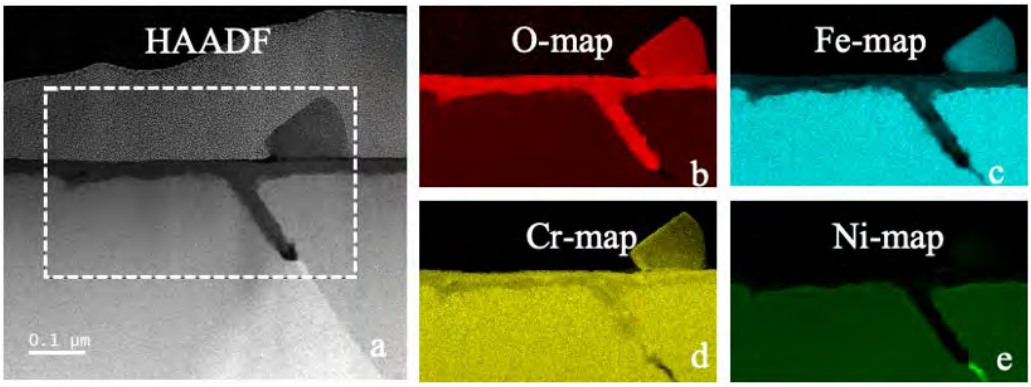

Figure 38. a) HAADF image showing an attacked HAGB in A84-1-1 (strained SA304 SS; 5.4 dpa); b-e are O-map, Fe-map, Cr-map, and Ni-map collected from the outlined region shown in a, respectively.

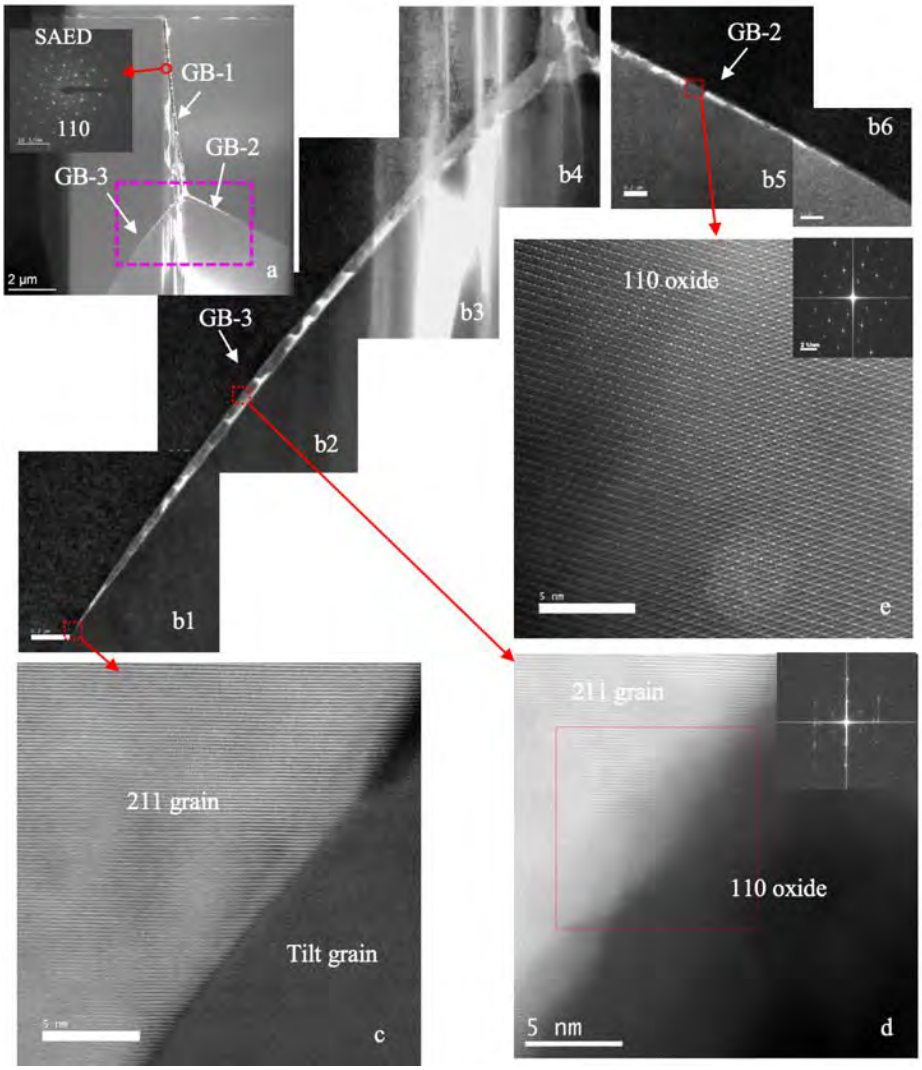

Figure 39. a) A low magnification STEM BF image showing a cracked triple junction in A84-1-1 (strained SA304 SS; 5.4 dpa) sample with a region outlined partially magnified to b1-b6 STEM BF images. High resolution HAADF images c, d and e were taken from the outlined regions in b1, b2 and b5, respectively. The insets in d and e are their corresponding FFTs. The SAED pattern in a) as an inset was taken from the circled region with an oxide particle and the left matrix.

To further characterize the microstructures and microchemistries of GB-2 and GB-3 shown in Figure 39 in A84-1-1 (strained SA304 SS; 5.4 dpa) sample, STEM-SI EELS/EDS was performed at several different regions. Figure 40 shows STEM-SI EDS data collected from the surface region near the cracked GB-1 in Figure 39. The data indicate that the surface was oxidized forming large, isolated Fe-rich oxide particles which was confirmed be the spinel phase and a continuous Cr-rich oxide layer with a Ni-rich oxide layer underneath as indicated by white arrows in the maps.

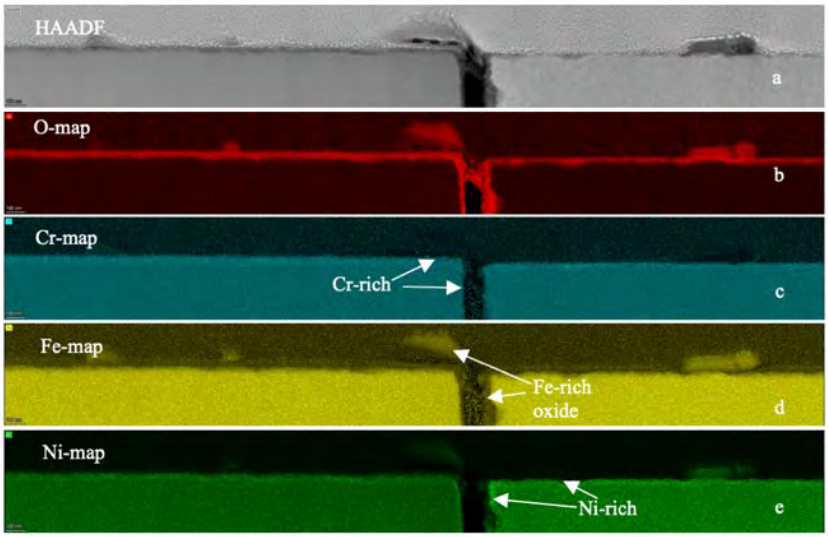

Figure 40. a) HAADF image showing the surface region of the cracked GB-1 in Figure 39 in A84-1-1 (strained SA304 SS 5.4 dpa) sample; b-e) are corresponding O-map, Cr-map, Fe-map and Ni-map, respectively.

Figure 41 displays STEM-SI EDS data collected from the GB-1 in Figure 39 in A84-1-1 (strained SA304 SS; 5.4 dpa) sample which shows the element distributions across the cracked GB. The data confirms that spinel oxide phase consisting of Fe, and Ni exists in the surface of the flanks of the cracked GB as island-like particles. A thin Cr-rich layer followed by a Ni-rich oxide layer seems to have formed underneath the spinel oxide layer as indicated by white arrows in the maps. The element profiles extracted from the yellow arrow line shown in g show that the region with the arrowhead above is the $(Cr,Ni)Fe_2O_4$ spinel oxide.

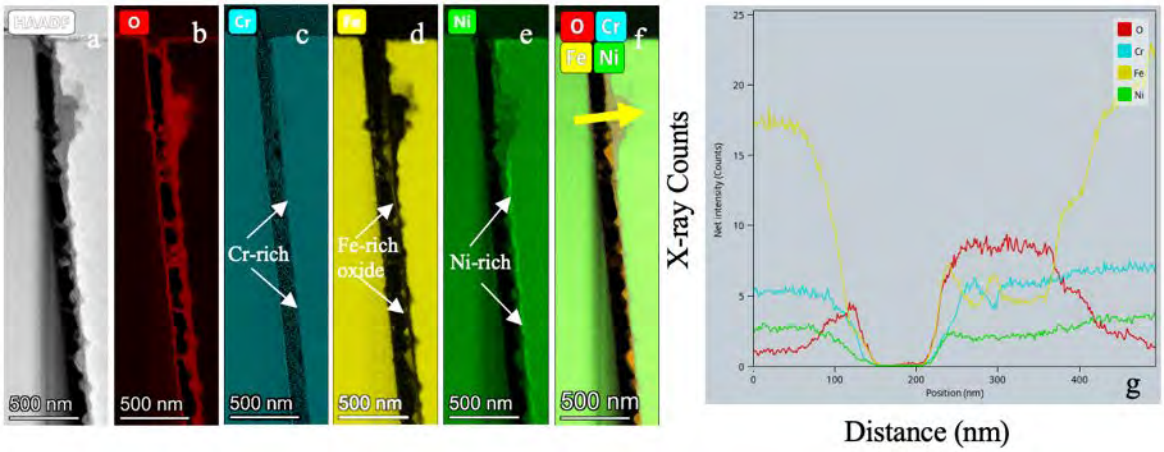

Figure 41. a) HAADF image showing the flank region of the cracked GB-1 in Figure 39 in A84-1-1 (strained 304 5.4 dpa) sample; b-f are corresponding O-map, Cr-map, Fe-map, Ni-map and mixed map, respectively. g) displays the element profiles across the crack along the yellow arrow line in f).

Figure 42 shows STEM-SI EELS data collected from the triple junction region in Figure 39. From the mixed Fe-Cr-Ni-O map shown in Figure 42b, we can clearly see that the cracked triple-junction GBs has a Fe-rich oxide core surrounded by a thicker Cr-rich oxide layer. In between the Cr-rich layer and the matrix grains, a very thin Ni layer was seen to form as indicated by white arrows in the maps.

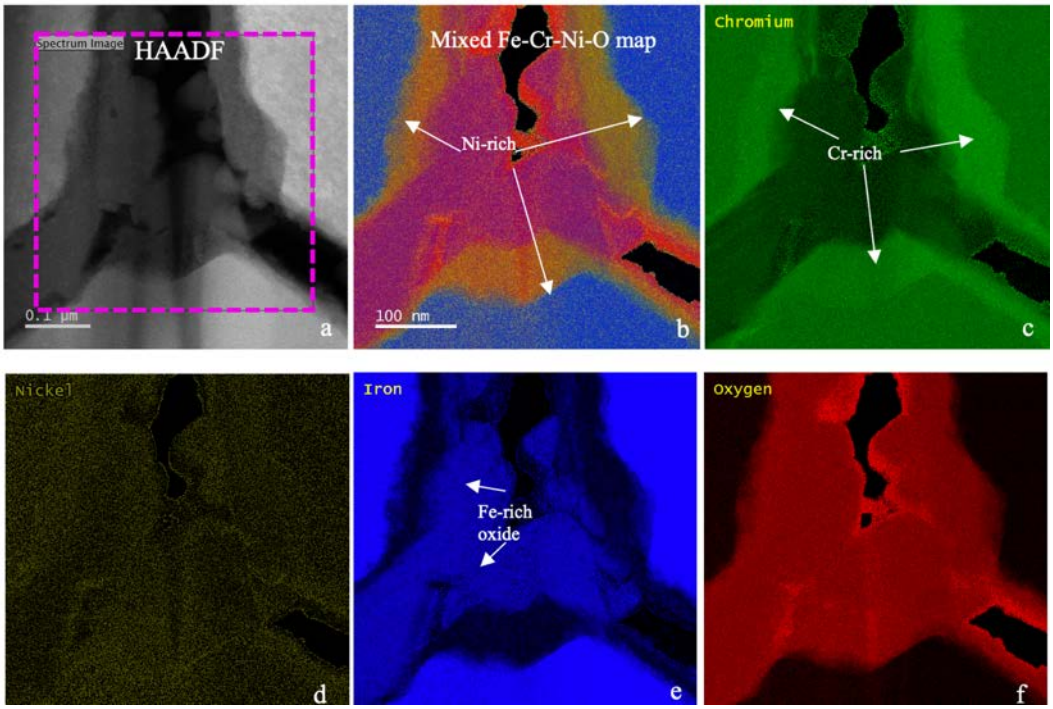

Figure 42. a) HAADF image showing the cracked triple junction in A84-1-1 (strained 304 SS 5.4 dpa) sample with a region outlined for STEM-SI EELS; b) is a mixed element map with its corresponding component Cr-map, Ni-map, Fe-map and O-map shown in c)-f), respectively.

Figure 43 shows STEM-SI EELS data collected from a region of the GB-3 in Figure 39 in A84-1-1 sample with cracked oxide. The colored element maps and the element profiles show that the oxide in the GB has a Fe-rich oxide core surrounded by a Cr-rich and then a Ni-rich oxide layer as indicated by white arrows in the maps.

STEM-SI EELS data collected from the GB-3 in Figure 39 in A84-1-1 sample at the crack tip region are shown in Figure 44. Element profiles were extracted along the yellow arrow direction locating about 30 nm above the crack tip. The data clearly show that the oxide phase has three layers, the spinel phase in the core, followed by a Cr-rich and then a Ni-rich layer as indicated by white arrows in the maps. From the O-map, it seems that oxygen has diffused beyond the crack tip (~ 30 nm) and Ni is enriched still deeper. This may also be due to the tilt of the cracked GB when performing imaging. More experiments are needed for clarifying this observation.

Figure 45 and Figure 46 show STEM-SI EELS data collected from the cack tip region and the GB region beyond the crack tip from the GB-3 in Figure 39 in A84-1-1 sample, respectively. It should be mentioned that those two datasets were collected after the sample had been further thinned by FIB. No oxygen was seen at the GB in the enhanced Ni-rich region and beyond. The imaged GB region in Fig. 46 has no oxygen either. This means oxygen has not diffused over the enhanced Ni-rich GB region. The GB shows RIS with

Ni segregation and Cr and Fe deficits after the enhanced Ni-rich region. The enriched region has Ni that is ~3.7 times higher over the RIS GB.

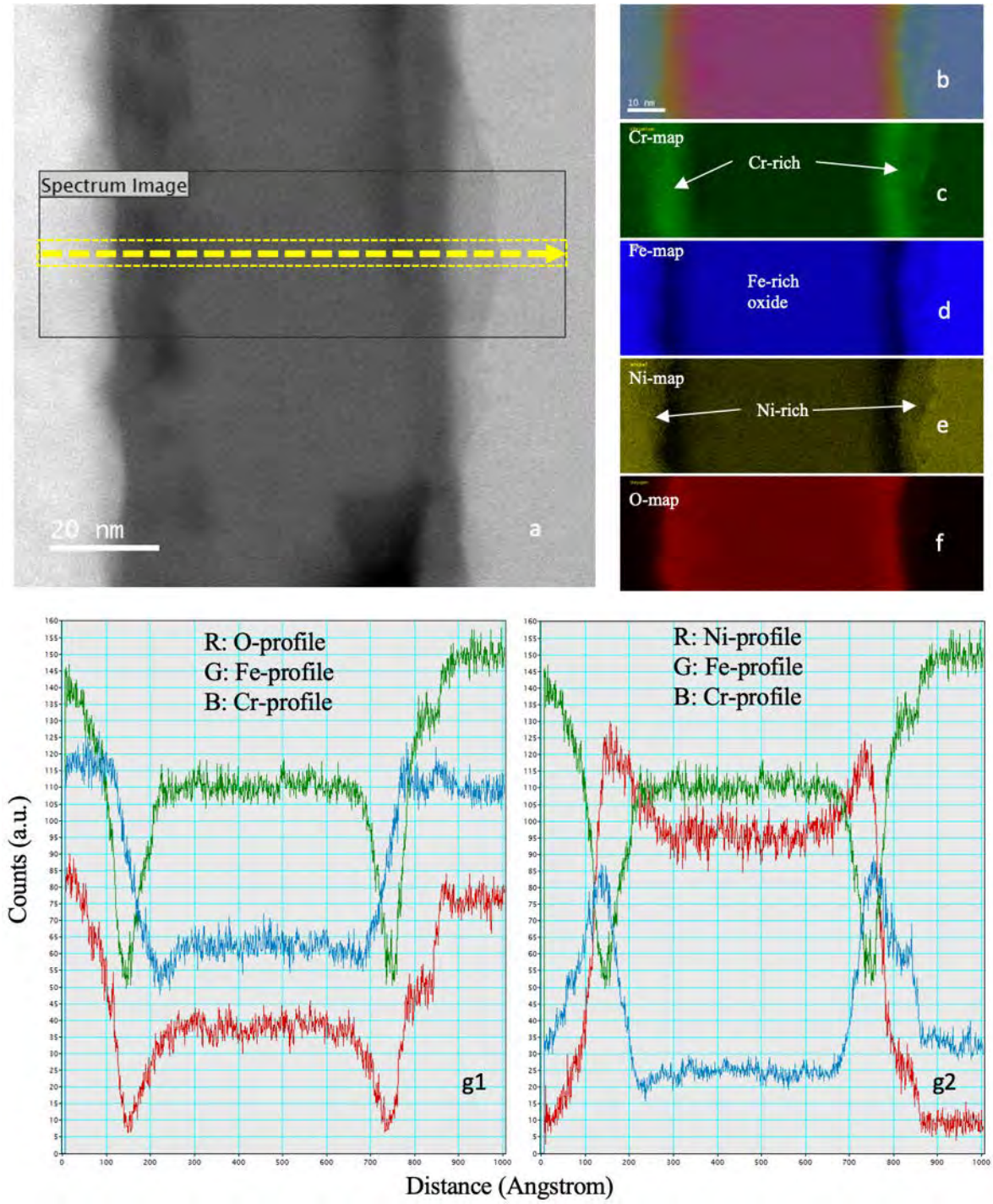

Figure 43. a) HAADF image showing a portion of the cracked GB-3 in Figure 39 in A84-1-1 (strained 303 SS; 5.4 dpa) sample with a region outlined for STEM-SI EELS and a yellow arrow for creating element profiles; b) is a mixed element map with its corresponding component Cr-map, Fe-map, Ni-map and O-map shown in c)-f), respectively; g1 and g2 show element profiles along the yellow arrow line direction in a).

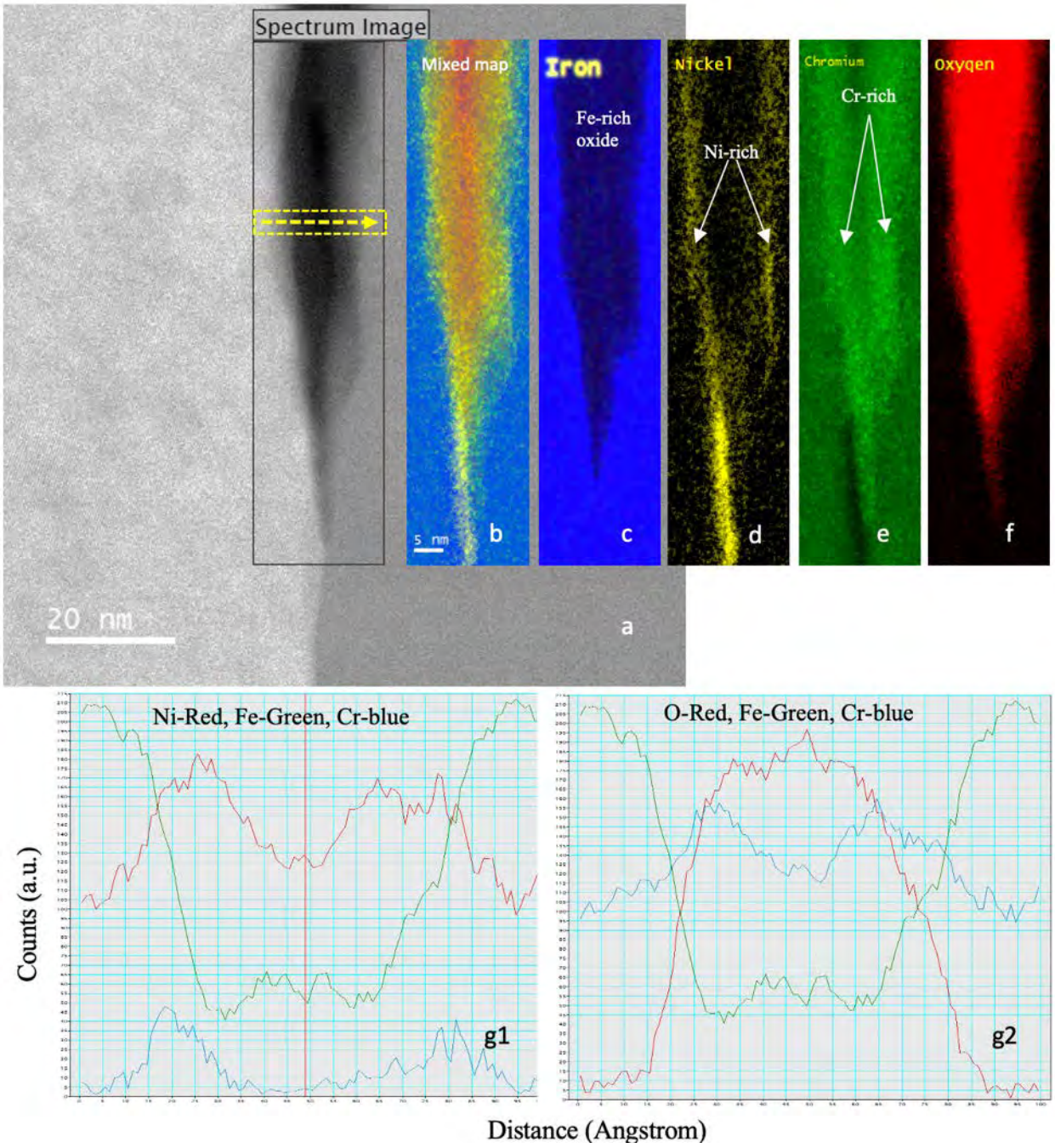

Figure 44. a) HAADF image showing the crack-tip region of the cracked GB-3 in A84-1-1 (strained 303 SS; 5.4 dpa) sample with a region outlined for STEM-SI EELS and a yellow arrow for creating element profiles; b) is a mixed element map with its corresponding component Fe-map, Ni-map, Cr-map and O-map shown in c)-f), respectively; g1 and g2 show element profiles along the yellow arrow line direction in a).

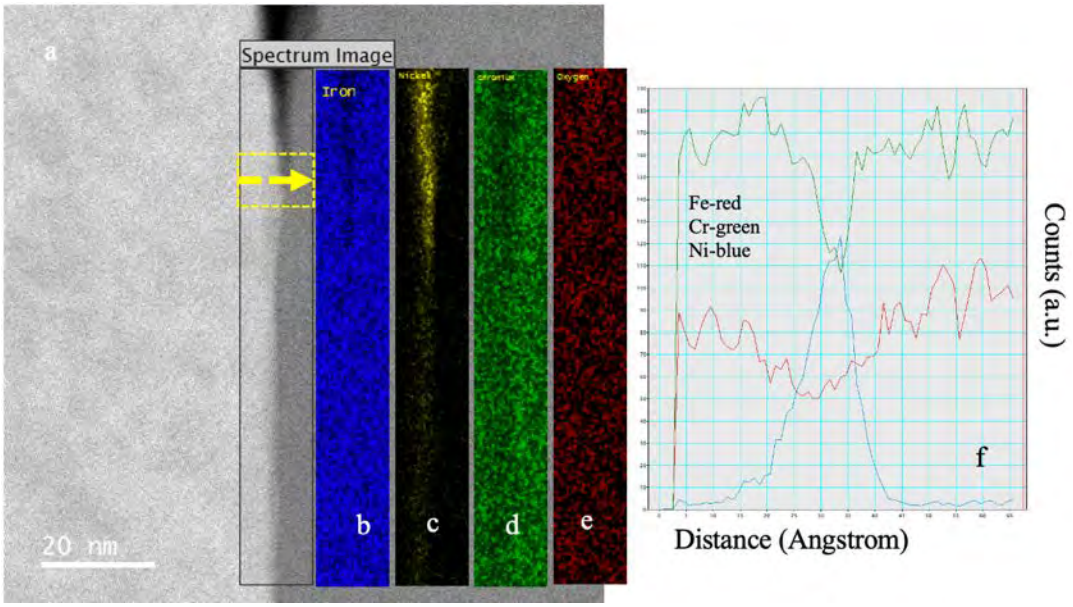

Figure 45. a) HAADF image showing the crack-tip region of the cracked GB-3 in Figure 39 in A84-1-1 (strained 304 SS; 5.4 dpa) sample with a region outlined for STEM-SI EELS and a yellow arrow for creating element profiles across the crack tip; Fe-map, Ni-map, Cr-map and O-map shown in b-e, respectively; f shows element profiles along the yellow arrow line direction in a).

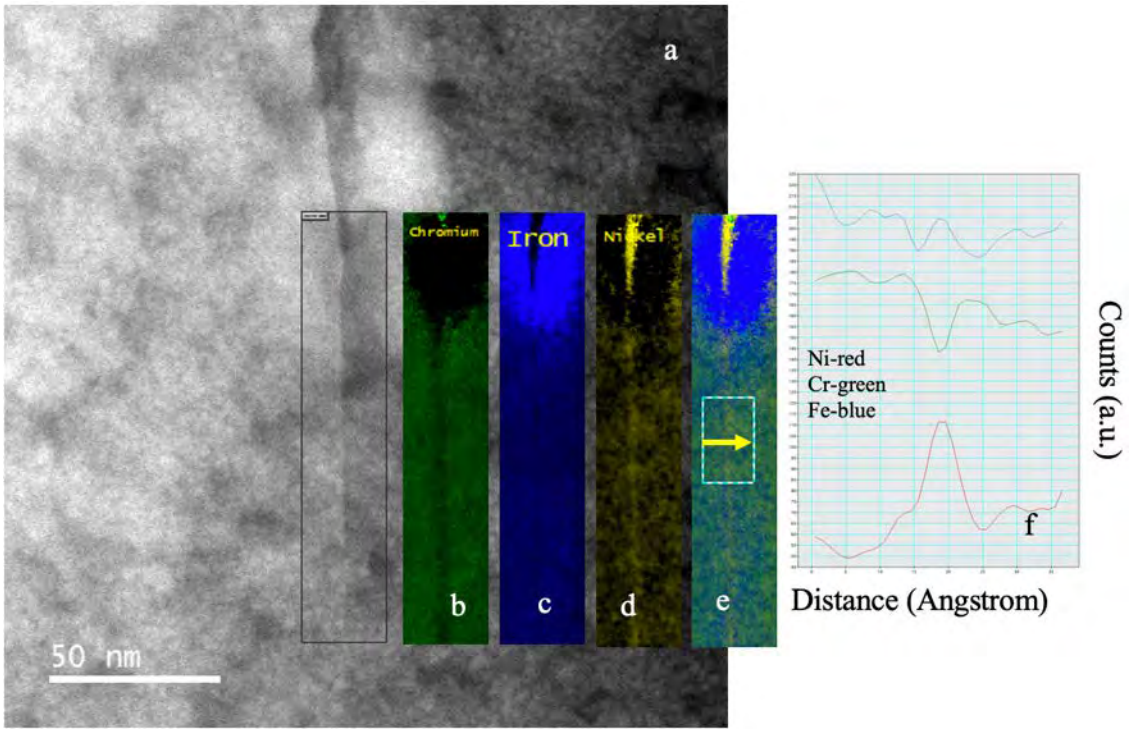

Figure 46. a) HAADF image showing the GB region beyond the crack tip of the cracked GB-3 in Figure 39 in A84-1-1 (strained 304 SS; 5.4 dpa) sample with a region outlined for STEM-SI EELS and a yellow arrow for creating element profiles across the GB ~50nm away from the crack tip; Cr-map, Fe-map, Ni-map and mixed-map shown in b-e, respectively; f shows element profiles along the yellow arrow line direction in a).

4. DISCUSSION

IASCC is a complex phenomenon in which the material properties, stress and water chemistry are simultaneously changed by irradiation. In the last 20 years, IASCC has been observed in structural components such as PWR baffle bolts and BWR core shrouds and top guides. Though extensive literature exists for this research field, a complete consensus on the underlying mechanism of cracking has not yet emerged [12, 13]. Recent studies have focused on the combination of high local stress/strain concentration at GB caused by heterogeneous deformation [14-17] and degradation of GB strength due to GB oxidation [18, 19]. In this present study, an attempt to identify the role of straining mode, grain boundary oxidation and localized deformation were carried out, also to elucidate the role of environments.

4.1 Effect of Straining Mode on IG Cracking

CW316 SS

Three different straining modes were used to perform the four-point bend tests in PWR primary water environment: single, interrupted, and constant load. An additional approach, the pre-oxidation in PWR primary water and subsequent straining in high temperature argon gas atmosphere, was also performed. At first, the results of single-strained CW316 SS (42 dpa) and interrupted-straining CW316 SS (125.4 dpa) were considered in evaluating the effect of these two straining modes on the cracking behavior. It should be noted that the irradiated yield strengths of the CW316 SS samples studied in this project did not have significant variation with dose range from 42 to 125.4 dpa. Table 10 summarizes the characteristics of cracking obtained through four-point bend testing of CW316 SS (neutron irradiated up to 125. 4 dpa). The sample B98-B1 (CW316 SS; 42 dpa) was single-strained to 0.5YS, whereas the sample B35-B1 (CW316 SS; 125.4 dpa) had multiple straining steps starting from 0.4 to 0.6 YS with stress increments of 0.05 YS. Note that both samples were strained at a constant strain rate of 4.3×10^{-8}/s in PWR primary water. Table 10 shows that the number of cracks and the crack density of both samples were comparable at a stress level of 0.5YS, but the average crack length of multiple-strained sample is much lower than that of the single-strained sample. Further, with increase of stress increment to 0.6YS, the multiple-straining sample showed a rapid increase in the number of new cracks but not the average crack length. This means, new crack formation or nucleation was favored relative to crack propagation in multiple straining mode. Overall, the 125.4 dpa multiple-strained sample was under load for ˜320 h or 4x that of the 42 dpa single-strained sample (~81 h). Thus, crack nucleation can be attributed to the longer period of exposure in PWR primary water, meaning that straining mode can affect crack nucleation significantly. In the single-straining test, cracking occurs only if the stress in the oxidized GBs meet the stress threshold. But, in the case of interrupted straining, oxidation of the GBs along with the emergence of DCs induce a greater number of cracks.

SA304 SS

Two modes of straining were compared here; interrupted straining mode, and constant load straining mode. Table 12 presents the quantitative cracking summary of SA304 SS samples (5.4 and 95 dpa), as each of them were tested in both interrupted as well as in constant load straining mode of in PWR primary water. In interrupted straining mode, the 5.4 dpa sample cracked at 0.6YS. With further increment of stress level up to 0.7YS, the number of cracks increased significantly. At low stress level (0.5YS), the 5.4 dpa sample tested in constant load mode for 200 h initiated cracks, suggesting that longer exposure time at low stress

level initiates cracking. It should be noted that the total exposure time of the interrupted-straining sample (i.e., 0.5, 0.6 and 0.7YS) is (˜207 h), which is almost equal to the constant load exposure test at 0.5YS (200 h). This means that in addition to the exposure time, straining history in the interrupted-straining mode promotes crack nucleation.

The 95 dpa sample that was strained twice to 0.6YS showed a greater number of cracks than the constant load mode tests conducted at 0.4 and 0.5YS. Apparently, the constant load mode drops the crack initiation stress to 0.5YS due to grain boundary oxidation, but straining twice at a higher stress level (0.6YS) increases crack nucleation. It must be noted that the total time spent at stresses 0.4YS (200 h) and 0.5YS (200 h) in constant load mode was 400 h, whereas in the case of interrupted straining twice to 0.6YS, the exposure time is around 225 h. Though the exposure time is much less than in the constant strain rate mode test, the observed cracking is high. This means that in addition to exposure time, straining history (i.e. number of interrupted straining steps with or without stress increments) plays a role in cracking nucleation. The results evidencing that straining mode plays a role in IG crack initiation.

4.2 Effect of Grain Boundary Oxidation and Localized Deformation on IG Cracking

Grain boundary oxidation is suspected as a possible causative factor in IASCC. The primary oxidizing element in 316 and 304 SS is Cr, and at exposure temperature 320 ℃ in PWR condition, the grain boundaries become the preferred site for oxidation. Thus, Cr-rich oxides are formed in the GBs, as shown in the Figure 19. In general, the following three factors could decrease GB strength or cohesion; GB segregation of impurities or solute elements, GB oxidation, and vacancies and micro-voids formation in the GB. It has been reported [19] that GB strength decreases with the progression of oxidation along the GBs of alloy 600, meaning that oxidation is an important factor affecting the GB strength. Figures 17 and 47 revealed that cracking in sample B98-B1(CW316 SS; 42 dpa) occurred only at the oxidized grain boundaries that are perpendicular to the straining direction, in agreement with prior studies [20, 21], and indicating that the normal stress plays a vital role in IG cracking [22]. The SA304 SS samples A84-1-2 (5.4 dpa), A96-1-1 (95 dpa) and A98-1-1 (69 dpa) that had been exposed for a longer period of time in PWR primary water showed a lower crack initiation stress of 0.5YS (see Table 12 and 14), which is indicative of increased degradation of GB cohesive strength with continued oxidation. Straining in constant load mode showed clearly that the oxidized grain boundaries due to longer exposure times ultimately leading to IG cracking even though the stresses were kept at a constant value. This tendency is consistent with the degradation of GB strength by oxidation in Alloy 600 exposed to simulated PWR primary water [18]. The micro tensile tests that were performed on Alloy 600 samples revealed that a lower fracture stress was obtained for a longer exposure time, i.e. intergranular fracture occurred at 180-300 MPa in samples that contained an oxidized GB and did not occur even at 1000 MPa in samples that contained a non-oxidized GB. In a similar manner, an occurrence of intergranular oxidation in Alloy 690 weakens the GB sufficiently to nucleate cracks, as the Cr-rich oxide produced along the GB is brittle, providing an easy pathway through the alloy [23].

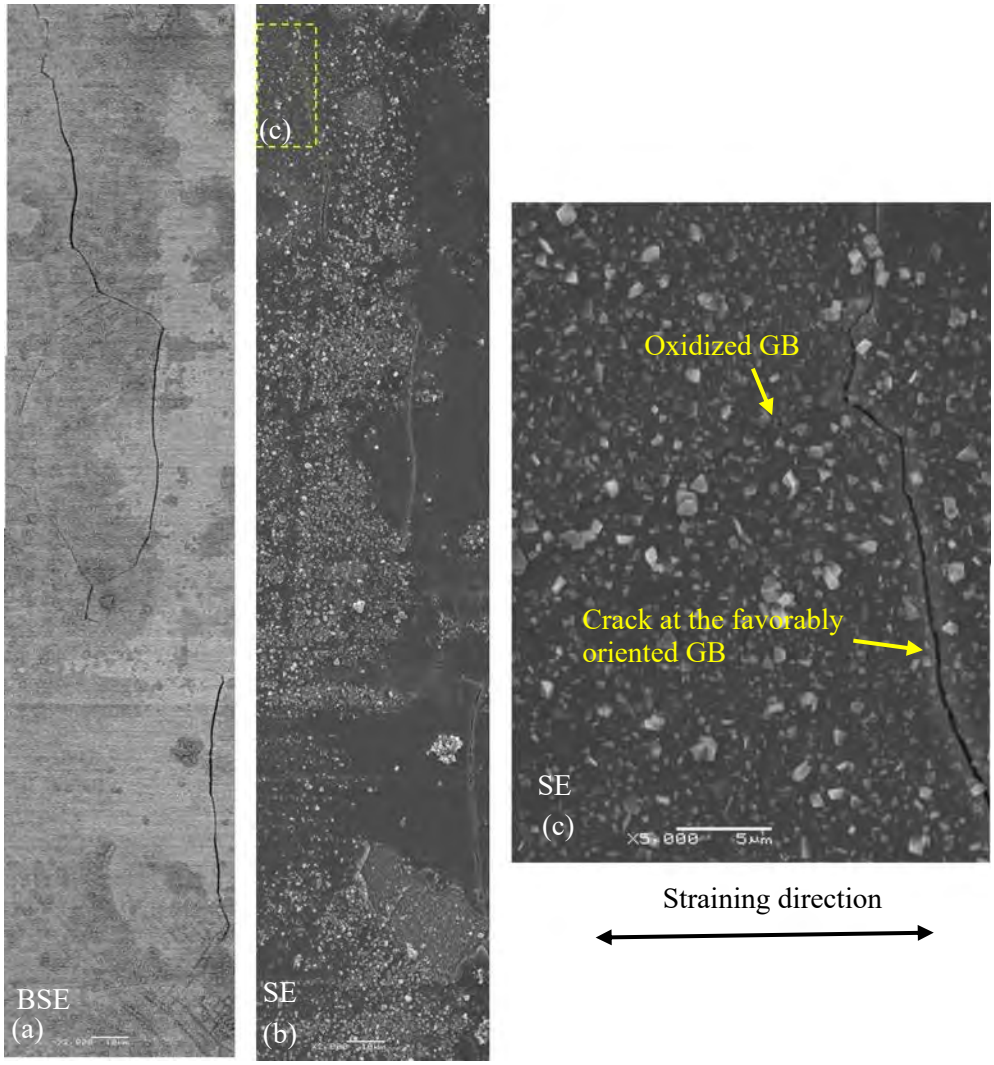

Figure 47. Stitched BSE and SE images shows the cracking of oxidized grain boundaries that are favorably oriented in CW316 SS (42 dpa).

Another interesting observation in constant load mode straining was the severe oxidation at the DC-GB intersections. The intersection of a dislocation channel with a grain boundary seems to enhance the oxidation locally at the GBs or triple junction (see Figures 23, 24 and 48). These are potential sites which can initiate cracks by rupturing the brittle nature GB oxides and the intergranular cracks found in SA304 SS that formed directly at the intersection between dislocation channels and grain boundaries are the best example of it. As shown in the Figure 25-27, when a dislocation channel impinges on the heavily oxidized grain boundary, crack initiation is promoted. During the course of constant load straining in high temperature water, grain boundaries were subjected to stresses that were due to the pile-up of dislocations at the boundary as well as those due to the applied load. This total grain boundary normal stress at the oxidized grain boundary is believed to be the cause of cracking at the DC-GB intersection site. The degree of stress concentration depends on the details of the GB defect structure and relaxation state [24].

No IG cracking was observed upon straining of a non-oxidized sample A98-3 (69 dpa) to 0.8YS (Figures 33 and 34) in high temperature argon which highlights the importance of oxidative environment on the cracking phenomena, meaning that merely deformations or other purely mechanical processes cannot be linked directly to IASCC. However, intergranular cracking occurs when the sample A98-1-1 (69 dpa) pre-oxidized in PWR primary water without load and then strained to 0.5YS in high temperature argon as shown in Figure 31 and 49. This experiment provides direct evidence that oxidation along grain boundaries during exposure in PWR primary water in the unstressed condition weakens GB strength which then leads to IG cracking during straining in high temperature argon. This proves that an aqueous corrosive environment is necessary for IASCC, and most importantly, GB oxidation ultimately lowering the stress required to crack the oxidized GB. The decrease in stress required to fracture oxidized GBs point towards mechanism where an oxide phase is first formed at GB, eventually reducing the stress threshold required to crack it.

It has also been proposed that the transmission of dislocations in the GB, result in slip of the GB that could also impact cracking [13, 25, 26] by fracture of the grain boundary oxide. However, grain boundary slip (sliding) has not been observed in irradiated stainless steels. McMurtrey et al. [20] found that the boundaries that did exhibited slip had a low incidence of cracking compared to those does not have slip.

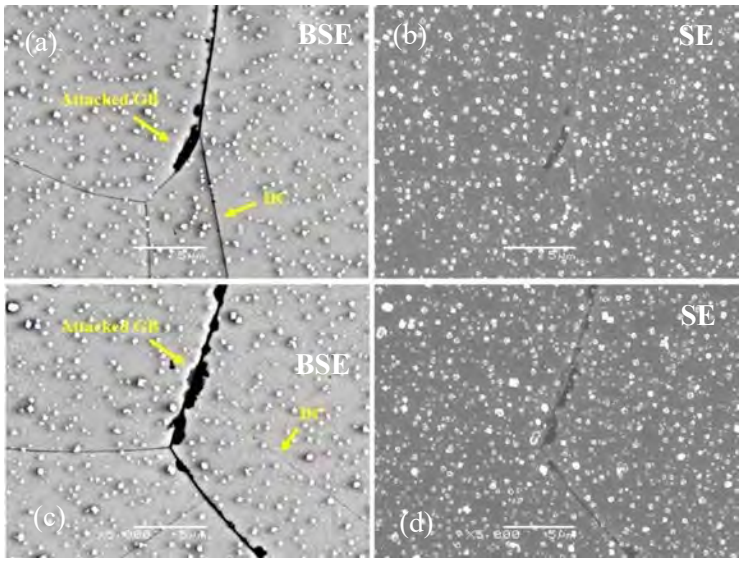

Figure 48. Intersection of a dislocation channel with grain boundary in constant load bend tested sample SA304 SS (5.4 dpa).

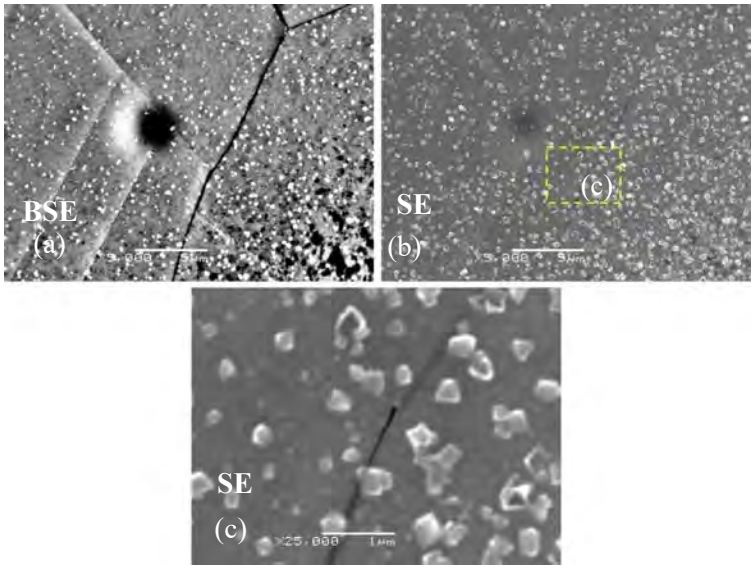

Figure 49. Crack initiation site where the DC terminate at the grain boundary and rupture the oxides, in a sample SA304 SS (5.4 dpa), pre-oxidized in PWR condition and strained to 50%YS in high temperature argon.

4.3 Linkage Between GB-Microstructure/Chemistry and Cracking

Results from the three CW-316 SS samples irradiated in reactor to 46.9 dpa, 67.4 dpa and 125.4 dpa show that they all have a high-density dislocation loops and Ni/Si-rich precipitates inside the grain matrix or at twin-boundaries. Strong Ni/Si segregation to the HAGBs were seen resulting in the formation of a Ni/Si rich layer along HAGBs that were depleted in Cr and Fe. There was little dependence of loop size and density, precipitates size and density and RIS level on damage level (dpa). The sizes, densities and distributions of loops and precipitates are very similar. The segregation level of Ni at GBs is the highest in the 46.9 dpa sample while the 125.4 dpa sample has the highest Si segregation at GBs. This may be interpreted as: 1) The segregation level of Ni and Si may depend on the types of GBs; 2) It may be a sampling issue that the data were collected from limited numbers of GBs.

For the strained neutron irradiated B35-B1 (CW316-SS 125.4 dpa) and A84-1-1 (304 SS 5.4 dpa) samples, both attacked and cracked HAGBs were observed. The surfaces of the two strained samples all have a thin Cr-rich oxide layer and large, isolated Fe-rich oxide particles above. For an attacked GB, the general structure features are that the two adjacent grains were oxidized separately and the original GB becomes the GB between the two oxides. The formed spinel oxides have growth relationships with the matrix. The oxidization starts from the surface of the sample and extends along the GB to a point where enhanced Ni segregation at the GB was found. Underneath the spinel-type oxide, there formed a Cr-rich oxide layer followed by a Ni-rich oxide layer for almost all the GBs (See in the Figures 37 and 38 in B35-B1 sample and Figures 40-44 in A840-1-1 sample).

Schematic drawings of the attacked and cracked GBs in B35-B1 (strained CW 316 SS 125.4 dpa) and A84-1-1 (strained 304 SS 5.4 dpa) samples have similar microstructures and microchemistry (as shown in Figure 50.) For the cracked GBs, the general features are that the GB has separated, forming shallow or deep gaps in between the two grains. There are still some oxide phases attached to the crack flanks, which

have a three-layer structure, i.e., Fe-rich spinel oxide, with a thin Cr-rich layer underneath followed by a thin Ni-rich layer against the grain face. Oxygen does not appear to have diffused beyond the crack-tip where enhanced Ni segregation was observed. The difference between B35-B1 (CW316 SS 125.4 dpa) sample and A84-1-1 (304 SS 5.4 dpa) sample is that the former has more Si which could still enrich in attacked GBs. Dislocation loops and precipitates have not been characterized for the 5.4 dpa 304 sample and so we cannot compare the difference in such microstructures in the two different alloys.

It should be noted that in both samples, at the tips of either attacked or cracked GBs, there formed enriched Ni regions that can extend from tens to several hundred nanometers along the GBs. The formation of Ni enriched regions is due to grain boundary migration (GBM) with different degrees of migration. Among those, the attacked GB in Figure 37 (f-j) shows more obvious GBM. This phenomenon has been observed in many alloys since it was first observed [27]. The feature is associated with preferential intergranular oxidation (PIO) ahead of crack tips which has been seen in many alloys as well as in the current studied alloys [28]. So, the formation of cracks in both the 304 and 316 SS is mostly due to the PIO mechanism [29, 30]. What should be noted is that all the FIB lift outs from GBs were cut from GBs with dislocation channels intersecting them (Figure 51). No cracks were seen from inclusions at GBs. The GB in Figure 51 a-b (also in Figure 36) is not normal to the sample surface, it is hard to see where the crack is along the GB. The GB shown in Figure 51 c-d (also in Figures 39-46) is almost perpendicular to the surface. Form the SE image in Figure 51d, it seems that the crack has occurred in the middle of the oxidized GB. This means that the oxidized GB, which was the original alloy GB, is the weakest site and is easy for crack to occur. This could be understandable considering microstructures and microchemistries of the studied attacked GBs, for example, the attacked GB shown in Figure 35.

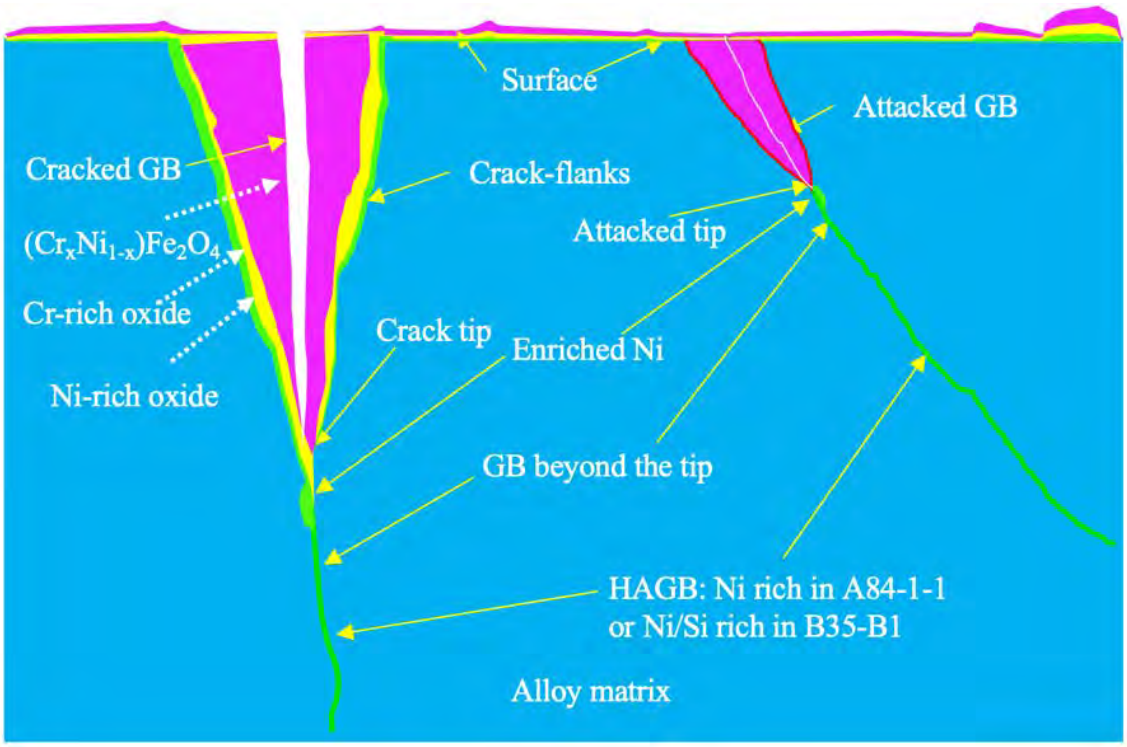

Figure 50. Schematic drawing summarizing the general features of the attacked and cracked GBs in B35-B1 (strained CW 316 SS; 125.4 dpa) sample and A84-1-1 (strained SA304 SS; 5.4 dpa) sample.

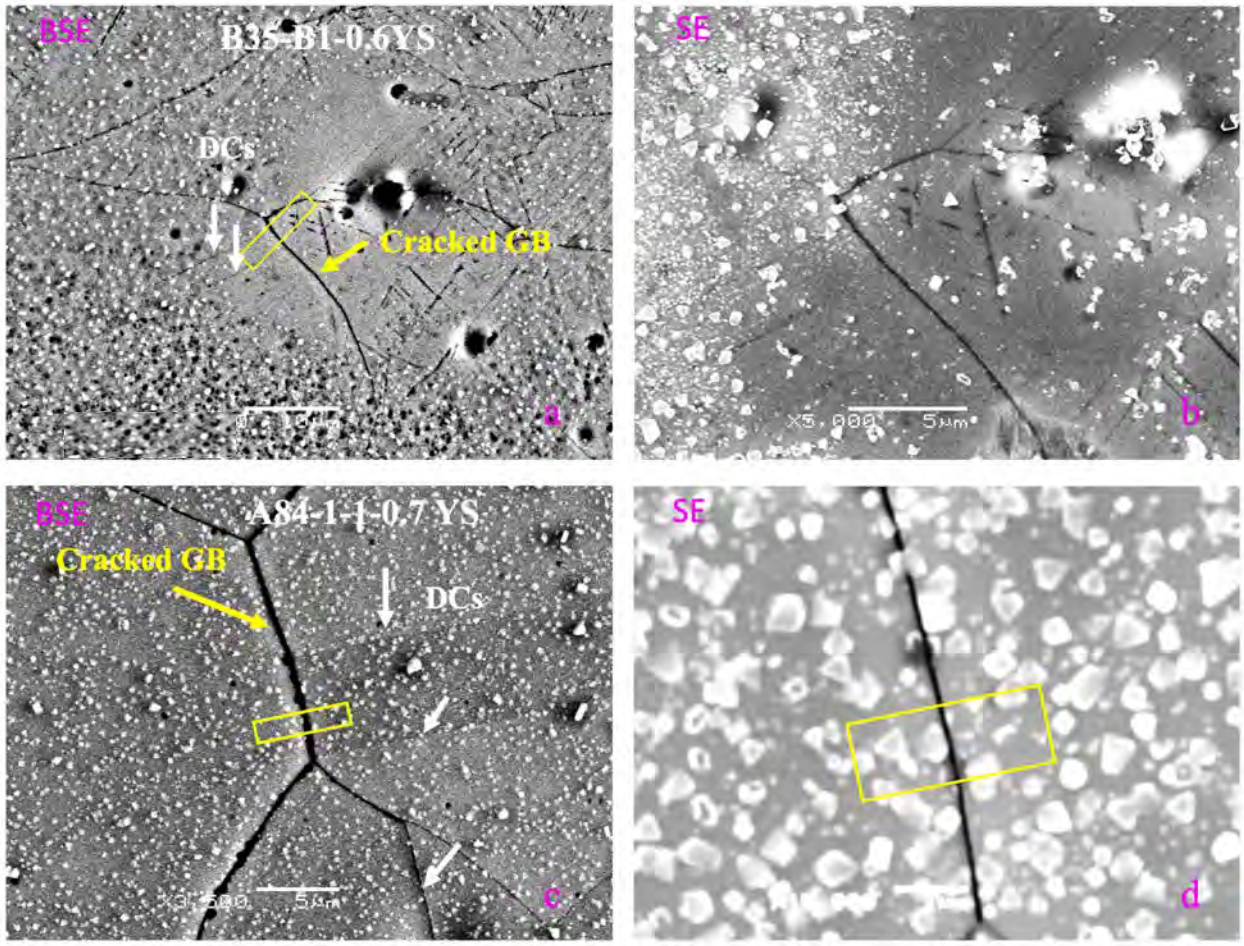

Figure 51. SEM BSE images showing the cracked GBs imaged in Figure 36 in B35-B1 (a) and the cracked GB imaged in Figures 39-46 in A84-1-1 (c), with their corresponding SE images shown in (b) and (d), respectively. The cracked GBs were pointed by yellow arrows and DLs were pointed by white arrows. FIB lift-outs were cut from the two highlighted yellow boxes.

5. CONCLUSIONS

IASCC is a complex process and numerous parameters can affect its emergence and severity, which can enhance or diminish certain effects. The influence of several methods of straining (such as single, interrupted, and constant load in four-point bend test) on IG cracking were studied. Furthermore, pre-oxidation in high temperature water and subsequent straining in an inert environment was conducted to separate the roles of load and environment on IG cracking.

Straining mode was found to significantly affect crack nucleation. In particular, the straining history is important. Multiple straining steps to the same fraction of yield strength will result in cracking at a lower value than in a single straining step. The constant load test method resulted in a lower crack initiation stress than dynamic straining to the same load, demonstrating that longer exposure time weakens the grain boundaries due to oxidation. The crack initiation stress for SA304 SS obtained from the constant load mode of straining was 0.5YS, whereas cracks initiated at 0.6YS in the interrupted straining mode. In addition,

stress concentration at the intersections of dislocation channels or slip bands with the grain boundaries or triple junctions acted as preferential sites for IG cracking.

Oxidation of the grain boundaries was observed to be a precursor to IG crack initiation. The role of grain boundary oxidation in IG cracking was established by separating the oxidation process from the loading process. Pre-oxidation in PWR water without application of load, followed by straining in an inert gas (Ar) resulted in cracking of the grain boundaries. Over long exposure times, the oxidation along grain boundaries weakens their strength and results in the initiation of IG cracks at a threshold stress. Cracks that are initiated at the intersections between dislocation channels and oxidized grain boundary remarkably indicates that localized deformation provides the amplification in stress which is high enough to fracture an oxidized grain boundary. Straining in pure Ar (without having any pre-exposure in high temperature water) verifies that the irradiated state is not inherently susceptible to IG fracture.

The oxides of cracked GBs have a three-layer structure consisting of Fe-rich spinel oxide as outer layer with a thin Cr-rich layer underneath followed by a thin Ni-rich layer. Ni is enriched at the oxide/metal interface and at the reaction front beyond the attacked GB. The formation of Ni enriched regions is due to grain boundary migration (GBM). The big difference between the CW 316 SS and SA304 SS is that the former has more Si and it enriches in attacked GBs. Cracks that initiated at grain boundaries were observed to occur within the GB oxide, indicating that it is the oxide itself that is fracturing rather than the oxide-matrix interface.

6. REFERENCES

[1] LWRS (2020) Milestone Report M2LW-20OR0402026.

[2] EPRI. CIR II Program: Description of the Boris 6 and 7 Experiments in the BOR-60 Fast Breeder Reactor. (2005).

[3] EPRI. Materials reliability program: A review of the cooperative irradiation assisted stress corrosion cracking research program (MRP-98). EPRI Report, vol. 10028072003.

[4] K.J. Stephenson, G.S. Was. The role of dislocation channeling in IASCC initiation of neutron irradiated stainless steel. J NUCL MATER. 481 (2016), 214-225.

[5] K.J. Stephenson. The role of dislocation channeling in IASCC initiation of neutron irradiated austenitic stainless steel. Ann Arbor: University of Michigan; 2016.

[6] G.W. HOLLENBERG, G.R. TERWILLIGER, R.S. GORDON. Calculation of Stresses and Strains in Four-Point Bending Creep Tests. J AM CERAM SOC. 54 (1971), 196-199.

[7] S.R. W. Critical analysis of “tight cracks”. CORROS REV. 28 (2010), 1-103.

[8] T. Malis, S.C. Cheng, R.F. Egerton. EELS log-ratio technique for specimen-thickness measurement in the TEM. J ELECTRON MICROSC Tech. 8 (1988), 193-200.

[9] D.J. Edwards, E.P. Simonen, S.M. Bruemmer. Evolution of fine-scale defects in stainless steels neutron-irradiated at 275 °C. J NUCL MATER. 317 (2003), 13-31.

[10] D. Du, K. Sun, G.S. Was. IASCC of neutron irradiated 316 stainless steel to 125 dpa. MATER. CHARACT. 173 (2021), 110897.

[11] L. Tan, R. E. Stroller, K. G. Field, Y. Yang, H. Nam, D. Morgan, B. D. Wirth, M. N. Gussev, J. T. Busby, Microstructural evolution of type 304 and 316 stainless steels under neutron irradiation at LWR relevant conditions, JOM 68 2016], 517.

[12] K. Fukuya. Current understanding of radiation-induced degradation in light water reactor structural materials. J NUCL SCI TECHNOL. 50 (2013), 213-254.

[13] G.S.Was, P.L. Andresen. Mechanisms behind irradiation-assisted corrosion cracking, NUCLEAR CORROSION (2020) 47-488. DOI: https://doi.org/10.1016/B978-0-12-823719-9.00003-2.

[14] M. Song, K.G. Field, R.M. Cox, G.S. Was. Microstructural characterization of cold-worked 316 stainless steel flux thimble tubes irradiated up to 100 dpa in a commercial Pressurized Water Reactor. J NUCL MATER. 541 (2020), 152400.

[15] M.N. Gussev, J.T. Busby. Deformation localization in highly irradiated austenitic stainless steels. Oak Ridge National Lab2014.

[16] T. Toyama, Y. Nozawa, W. Van Renterghem, Y. Matsukawa, M. Hatakeyama, Y. Nagai, A. Al Mazouzi, S. Van Dyck. Irradiation-induced precipitates in a neutron irradiated 304 stainless steel studied by three-dimensional atom probe. J NUCL MATER. 418 (2011), 62-68.

[17] Z. Jiao, G.S. Was. Localized deformation and IASCC initiation in austenitic stainless steels. J NUCL MATER. 382 (2008), 203-209.

[18] K. Fukuya, H. Nishioka, K. Fujii, T. Miura, Y. Kitsunai. Local strain distribution near grain boundaries under tensile stresses in highly irradiated SUS316 stainless steel. J NUCL MATER. 432 (2013), 67-71.

[19] K. Fujii, T. Miura, H. Nishioka,K. Fukuya. Degradation of grain boundary strength by oxidation in alloy 600, in: J.T. Busby, G. Ilevbare, P.L. Andresen (Eds.), Proceedings of the 15th International Conference on Environmental Degradation of Materials in Nuclear Power Systems-Water Reactors, The Minerals, Metals & Materials Society, Colorado, 2011, p. 1447-1458.

[20] M.D. McMurtrey, B. Cui, I.M. Robertson, D. Farkas, G.S. Was. Mechanism of dislocation channel-induced irradiation assisted stress corrosion crack initiation in austenitic stainless steel. Current Opinion in Solid State and Materials Science. 19 (2015), 305-314.

[21] G.S. Was, D. Farkas, I.M. Robertson. Micromechanics of dislocation channeling in intergranular stress corrosion crack nucleation, Current Opinion in Solid State and Materials Science. 16 (2012), 134-142.

[22] D.C. Johnson, B. Kuhr, D. Farkas, G.S. Was. Quantitative linkage between the stress at dislocation channel – grain boundary interaction sites and irradiation assisted stress corrosion crack initiation. ACTA MATER. 170 (2019), 166-175.

[23] T. Moss, W. Kuang, G.S. Was, Stress corrosion crack initiation in Alloy 690 in high temperature water, Current Opinion in Solid State and Materials Science, 22 (2018) 16-25.

[24] B.Kuhr, D. Farkas, I.M. Robertson, D. Johnson, G.S.Was, Stress localization resulting from grain boundary dislocation interactions in relaxed and defective grain boundaries, Metallurgical and Materials Transactions A 51A (2020) 667-683.
[25] E.A. West. Influence of local stress and strain on intergranular cracking of 316L stainless steel in supercritical water. Ann Arbor: University of Michigan; 2010.
[26] W. Lai, Z. Jiao, G.S. Was. Effect of environment and prestrain on IASCC of austenitic stainless steels. (2011), 1397-1412.
[27] R.W. Balluffi, J.W. Cahn. Mechanism for diffusion induced grain boundary migration. Acta Metall. 29(1981) 493-500.
[28] T.J. Rupert, D.S. Gianola, Y. Gan, K.J. Hemker. Experimental observations of stress-driven grain boundary migration. Science 326 (2009) 1686-1690.
[29] L.Volpe, M.G. Burke, F. Scenini. Understanding the role of diffusion induced grain boundary migration on the preferential intergranular oxidation behavior of alloy 600 via advanced microstructural characterization. Acta Materialia 175 (2019) 238-249.
[30] Z. Chen, K. Arioka, S. Lozano-Perez. A study on the diffusion-induced grain boundary migration ahead of stress corrosion cracking crack tips through advanced characterization. Corrosion Science 183 (2021) 109328.